

Improved Characterization of Far-Regional and Near-Teleseismic Phases Observed in Central Asia

**Aaron Ferris
Anastasia Stroujkova
Katherine Murphy
Delaine Reiter**

**Weston Geophysical Corporation
181 Bedford Street, Suite 1
Lexington, MA 02420**

Final Report

2 July 2010

APPROVED FOR PUBLIC RELEASE; DISTRIBUTION IS UNLIMITED.



**AIR FORCE RESEARCH LABORATORY
Space Vehicles Directorate
29 Randolph Rd
AIR FORCE MATERIEL COMMAND
HANSCOM AFB, MA 01731-3010**

NOTICES

Using Government drawings, specifications, or other data included in this document for any purpose other than Government procurement does not in any way obligate the U.S. Government. The fact that the Government formulated or supplied the drawings, specifications, or other data does not license the holder or any other person or corporation; or convey any rights or permission to manufacture, use, or sell any patented invention that may relate to them.

This report was cleared for public release and is available to the general public, including foreign nationals. Qualified requestors may obtain copies of this report from the Defense Technical Information Center (DTIC) (<http://www.dtic.mil>). All others should apply to the National Technical Information Service.

AFRL-RV-HA-TR-2010-1059 HAS BEEN REVIEWED AND IS APPROVED FOR PUBLICATION IN ACCORDANCE WITH ASSIGNED DISTRIBUTION STATEMENT.

//signature//

ROBERT J. RAISTRICK
Contract Manager

//signature//

Domenic Thompson, Maj, USAF, Chief
Battlespace Surveillance Innovation Center

This report is published in the interest of scientific and technical information exchange, and its publication does not constitute the Government's approval or disapproval of its ideas or findings.

| REPORT DOCUMENTATION PAGE | | | | Form Approved OMB No. 0704-0188 | |
|--|--------------------|--------------------------------|---------------------------------------|---|---|
| Public reporting burden for this collection of information is estimated to average 1 hour per response, including the time for reviewing instructions, searching existing data sources, gathering and maintaining the data needed, and completing and reviewing this collection of information. Send comments regarding this burden estimate or any other aspect of this collection of information, including suggestions for reducing this burden to Department of Defense, Washington Headquarters Services, Directorate for Information Operations and Reports (0704-0188), 1215 Jefferson Davis Highway, Suite 1204, Arlington, VA 22202-4302. Respondents should be aware that notwithstanding any other provision of law, no person shall be subject to any penalty for failing to comply with a collection of information if it does not display a currently valid OMB control number. PLEASE DO NOT RETURN YOUR FORM TO THE ABOVE ADDRESS. | | | | | |
| 1. REPORT DATE (DD-MM-YYYY) 02-07-2010 | | 2. REPORT TYPE Final Report | | 3. DATES COVERED (From - To) 2-Nov-2005 to 30 Apr 2010 | |
| 4. TITLE AND SUBTITLE Improved Characterization of Far-Regional and Near-Teleseismic Phases Observed in Central Asia | | | | 5a. CONTRACT NUMBER FA8718-06-C-0002 | |
| | | | | 5b. GRANT NUMBER | |
| | | | | 5c. PROGRAM ELEMENT NUMBER 62601F | |
| 6. AUTHOR(S) Aaron Ferris, Anastasia Stroujkova, Katherine Murphy and Delaine Reiter | | | | 5d. PROJECT NUMBER 1010 | |
| | | | | 5e. TASK NUMBER SM | |
| | | | | 5f. WORK UNIT NUMBER A1 | |
| 7. PERFORMING ORGANIZATION NAME(S) AND ADDRESS(ES) Weston Geophysical Corporation 181 Bedford St., Suite 101 Lexington, MA 02420 | | | | 8. PERFORMING ORGANIZATION REPORT NUMBER | |
| 9. SPONSORING / MONITORING AGENCY NAME(S) AND ADDRESS(ES) Air Force Research Laboratory AFRL/RVBYE 29 Randolph Rd. Hanscom AFB, MA 01731 | | | | 10. SPONSOR/MONITOR'S ACRONYM(S) AFRL/RVBYE | |
| | | | | 11. SPONSOR/MONITOR'S REPORT NUMBER(S) AFRL-RV-HA-TR-2010-1059 | |
| 12. DISTRIBUTION / AVAILABILITY STATEMENT Approved for Public Release; Distribution Unlimited. | | | | | |
| 13. SUPPLEMENTARY NOTES | | | | | |
| 14. ABSTRACT The early body-wave coda of far-regional events (14°– 29° degrees) contains triplicated arrivals from upper-mantle discontinuities that could potentially improve seismic monitoring capabilities. However, far-regional seismograms are typically under-utilized in location and magnitude estimation because path-specific heterogeneity and multiple phase interactions make the arrival suite difficult to interpret accurately. In this report we present a set of techniques that were developed to improve phase characterization and identification at these distances. We have applied our techniques to data from two arrays in Kazakhstan: MKAR (Makanchi) and KKAR (Karatau), both of which record far-regional events throughout south-central Asia. Our techniques include improved array processing methods (e.g., phase-coherence semblance stacking) to characterize arrival time, back-azimuth and slowness of individual phases within the P-coda arrival suite, and methods to more accurately identify the measured arrivals (e.g., τ -p transformation and clustering analysis to determine wavefield templates). | | | | | |
| 15. SUBJECT TERMS Seismic triplications, Mantle transition zone, Phase identification | | | | | |
| 16. SECURITY CLASSIFICATION OF: | | | 17. LIMITATION OF ABSTRACT SAR | 18. NUMBER OF PAGES 68 | 19a. NAME OF RESPONSIBLE PERSON Robert Raistrick |
| a. REPORT UNC | b. ABSTRACT UNC | c. THIS PAGE UNC | | | 19b. TELEPHONE NUMBER (include area code) 781-377-3726 |

Table of Contents

| | |
|---|-----------|
| 1. Project Summary | 1 |
| 2. Far-Regional Seismicity Observed at the KKAR and MKAR Seismic Arrays | 4 |
| 2.1 Zone 1: Iran and Caspian | 4 |
| 2.2 Zone 2: Southern Pakistan | 8 |
| 2.3 Zone 3: Northern Pakistan and Afghanistan | 9 |
| 2.4 Zone 4: Tibet | 10 |
| 2.5 Zone 5: Eastern Tarim Basin..... | 11 |
| 2.6 Zone 6: Western Mongolia..... | 11 |
| 2.7 Zone 7: Central Mongolia | 12 |
| 2.8 Zone 8: Baikal Rift Zone..... | 13 |
| 3. Phase Characterization Using Small-Aperture Regional Arrays | 13 |
| 4. Phase-Weighted Semblance Stacking of Small-Aperture Array Observations..... | 17 |
| 5. Wavefield Continuation Analysis to Determine Path-Specific 1-D Velocity Models | 23 |
| 5.1 Direct Inversion of Delay-Time and Slowness Array Measurements | 25 |
| 5.2 Wavefield Continuation Analysis Using Array Beams | 27 |
| 6. Examination of Region-Specific Phase Behavior Using Waveform Clustering..... | 33 |
| 7. Studies of Near-Array Earth Structure..... | 44 |
| 7.1 Near-Array Earth Structure from Receiver Functions | 45 |
| 7.2 Analysis of the PcP Phase | 49 |
| References..... | 53 |
| Appendix 1: Altering Small-Aperture Array Geometry to Improve Phase-Velocity | |
| Estimation..... | 57 |

List of Figures

| | |
|---|----|
| Figure 1. P/Pn phase residuals from ISC bulletins in Asia (1999-2001) as a function of epicentral distance . | 1 |
| Figure 2. Map of south-central Asia showing the location of the Makanchi (MKAR) and Karatau (KKAR) arrays in Kazakhstan . | 3 |
| Figure 3. Far-regional seismicity (14 - 18°) from the KKAR and MKAR arrays.. | 5 |
| Figure 4. Seismicity in Iran and the Caspian Sea region..... | 6 |
| Figure 5. Focal mechanism for Iran and the Caspian Sea region | 7 |
| Figure 6. Reference map of Pakistan and Afghanistan..... | 8 |
| Figure 7. Seismicity in northern Pakistan, Pamir Hindu Kush and Uzbekistan | 9 |
| Figure 8. Zone 4 and Zone 5..... | 11 |
| Figure 9. Map of regional seismicity for Mongolia and the Baikal Rift Zone | 12 |
| Figure 10. Temporal frequency versus spatial frequenc..... | 14 |
| Figure 11. MKAR array response function..... | 16 |
| Figure 12. KKAR array response function. | 17 |
| Figure 13. Slowness and back-azimuth slices through 3-D vespagrams | 20 |
| Figure 14. Profiles through the back-azimuth vespagram slices | 21 |
| Figure 15. Example of phase coherence semblance stack analysis. | 23 |
| Figure 16. Illustration of the behavior of turning rays..... | 24 |
| Figure 17. Sample τ - p data from the MKAR array..... | 26 |
| Figure 18. τ - p inversion for a velocity profile | 27 |
| Figure 19. Map of events used to construct a record section..... | 29 |
| Figure 20. Record section of the data f..... | 29 |
| Figure 21. Slant stack of the preprocessed data from the record section..... | 30 |
| Figure 22. Velocity-depth model results following downward continuation. | 31 |
| Figure 23. Results from applying wavefield continuation to earthquake data. | 32 |
| Figure 24. Comparison of the velocity-depth profile from wavefield continuation | 33 |
| Figure 25. 4 earthquakes recorded at MKAR that exhibit similar phase arrival characteristics .. | 34 |
| Figure 26. An example cluster group found from processing 167 array beams. | 36 |
| Figure 27. Wavefield clustering to generate a wavefield template..... | 38 |
| Figure 28. Template beams from the cluster analysis of 80 MKAR recorded events. | 39 |
| Figure 29. Velocity model used to generate synthetic waveforms. | 40 |
| Figure 30. Example synthetic seismograms for the waveform template-fitting grid search. | 41 |
| Figure 31. Example of the waveform fitting for template beam number 2 | 42 |
| Figure 32. Example of waveform fitting for template beam number 3. | 43 |
| Figure 33: Back-azimuth residuals found from polarization analysis | 45 |
| Figure 34. Synthetic receiver functions images for a 10° dipping Moho over a half-space | 46 |
| Figure 35. Azimuthal distribution of teleseismic events. | 47 |
| Figure 36. MKAR receiver-function record sections. | 48 |
| Figure 37. KKAR receiver-function record sections | 48 |
| Figure 38. Behavior of the PcP phase at far-regional distances | 50 |

| | |
|---|----|
| Figure 39. Spectrogram of a seismogram window around the predicted PcP phase (zero time). | 51 |
| Figure 40. Phase-weighted semblance stacking for PcP arrivals | 51 |
| Figure A-1. Current configuration of the KKAR array | 58 |
| Figure A-2. Synthetic array gather for the current configuration of KKAR and three additional hypothetical stations..... | 59 |
| Figure A-3. Vespagram analysis of the P arrivals in the synthetic waveforms | 59 |
| Figure A-4. Vespagrams for the P arrival using the five outer elements of the array..... | 61 |
| Figure A-5. Profile comparisons of the vespagrams..... | 62 |

1. Project Summary

In this project we investigated the behavior of early body-wave coda observed at intermediate distances from events in Central Asia. At these distances ($\sim 14^\circ - 29^\circ$ degrees) the waveforms contain triplicated arrivals from upper-mantle discontinuities that could potentially improve seismic monitoring capabilities. However, intermediate-distance observations are typically under-utilized in location and magnitude estimation, because heterogeneity along the path and complicated phase interactions make the body-wave arrival suite difficult to interpret.

The phase complexities that occur at distances between $13 - 30^\circ$ produce uncertainties and errors in the phase picks in seismic bulletins. We demonstrate this phenomenon in Figure 1, in which we plotted Pn/P travel-time residuals as a function of epicentral distance. To generate this figure, we retrieved International Seismic Centre (ISC) bulletins for the years 1999-2001 from the Flinn-Engdahl Seismic Regions 26-30, 47 and 48 (see <http://neic.usgs.gov/neis/epic/fer.html>), which include most of Asia and parts of the Middle East. We included all events with ISC depths less than 40 km that were located by more than 25 stations. In Figure 1a, we plotted the residuals (gray dots) with respect to the IASPEI91 (Kennett and Engdahl, 1991) model for associated first-arriving P -wave picks between $10 - 30^\circ$. Then we calculated the density (number) of residual picks in boxes of 0.5° distance by 0.5 seconds of residual, and superposed a smoothed version of the resulting image over the individual picks. We also plotted two dashed black lines in Figure 1a that show the travel-time differences between branches $C'B' - A'B'$ and $CB - AB$, with the corresponding ray diagrams and travel-time branches shown in Figure 1b.

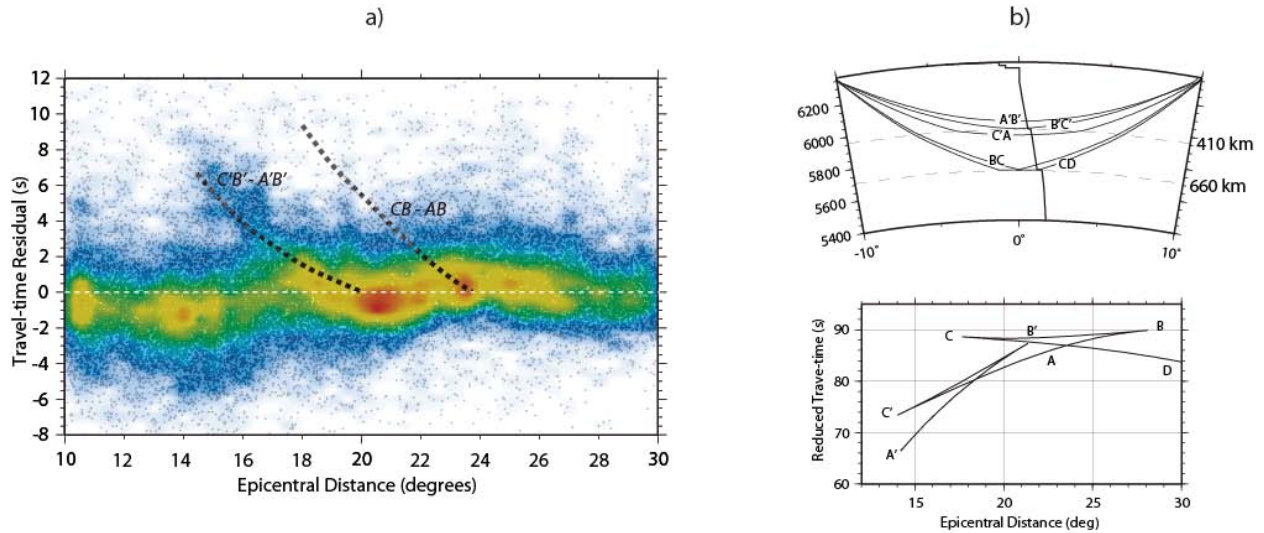


Figure 2. a) P/Pn phase residuals (with respect to the IASPEI91 model) from ISC bulletins in Asia (1999-2001) as a function of epicentral distance; the residual density as a function of distance and reduced travel time is shown as a superposed color image. Heavy black dashed lines show the travel-time difference between secondary and primary upper-mantle phase branches of the *iasp91* travel-time curves, shown in b).

Figure 1a clearly shows a large cloud of travel-time residuals that are associated with the 410-km triplication (occurring at $14 - 18^\circ$ distance). There is also considerable structure to the residuals in the regional to far-regional range, revealed by the negative residual bias at distances between $10 - 17^\circ$. While this particular data set does not reveal an increase in phase residuals associated with the 660-km discontinuity (i.e., the *CB* travel-time branch), we have observed such an effect for other time ranges and in other bulletins (e.g., National Earthquake Information Center [NEIC]). This type of residual behavior as function of epicentral distance is also present in the phase picks used to *locate* events at the ISC, but other agencies restrict their location travel-time picks more aggressively, making the phenomenon shown in Figure 1a less apparent.

The large arrival-time residual patterns displayed in Figure 1 provided the original motivation for our research project. The pattern of the residuals suggested that multi-pathing effects from the 410-km and 660-km discontinuities causes phase arrivals to be systematically mispicked and/or mislabeled. Triplication effects from multi-pathing produce amplitude and arrival phenomena that result in uncertainties and errors in the phase picks in seismic bulletins.

To address these issues, we developed a set of characterization techniques for phases observed at intermediate distances, combined with studies of Earth structure along paths sampling upper-mantle transition zone structure in Central Asia. We have applied our techniques to data from two arrays in Kazakhstan: MKAR (Makanchi) and KKAR (Karatau), both of which record far-regional events from most of south-central Asia (see Figure 2). To provide a test bed for our analysis techniques, we collected waveform data for moderate-sized events observed at the MKAR and KKAR arrays. We populated the database with events that were well located teleseismically and had Global Centroid Moment Tensor (CMT) solutions (<http://globalcmt.org>) associated with them. In total we collected waveforms on 600 events that appear in the EHB bulletin (Engdahl *et al.*, 1998) for the years 2002 through 2006. Figure 2 shows the EHB locations for these events, which have epicenter distances ranging between 14° and 29.7° from at least one of the arrays. Most of the events are located in the Middle East and Southern Asia, extending through Mongolia to southern Siberia. There are no events to the north-northwest of the arrays in the database, due to lack of seismicity in these regions at the intermediate distance range. The database contains 296 events recorded at MKAR and 304 events recorded at KKAR, with an additional 118 events that are in the intermediate distance range at both KKAR and MKAR. Magnitudes vary between $m_b = 4.0 - 6.8$, with most events below an m_b of 5.8. Events depths are mostly constrained to the crust, but there are some events with hypocentral depths up to 150 km deep. There are only 38 events in the database that have depths greater than 38 km.

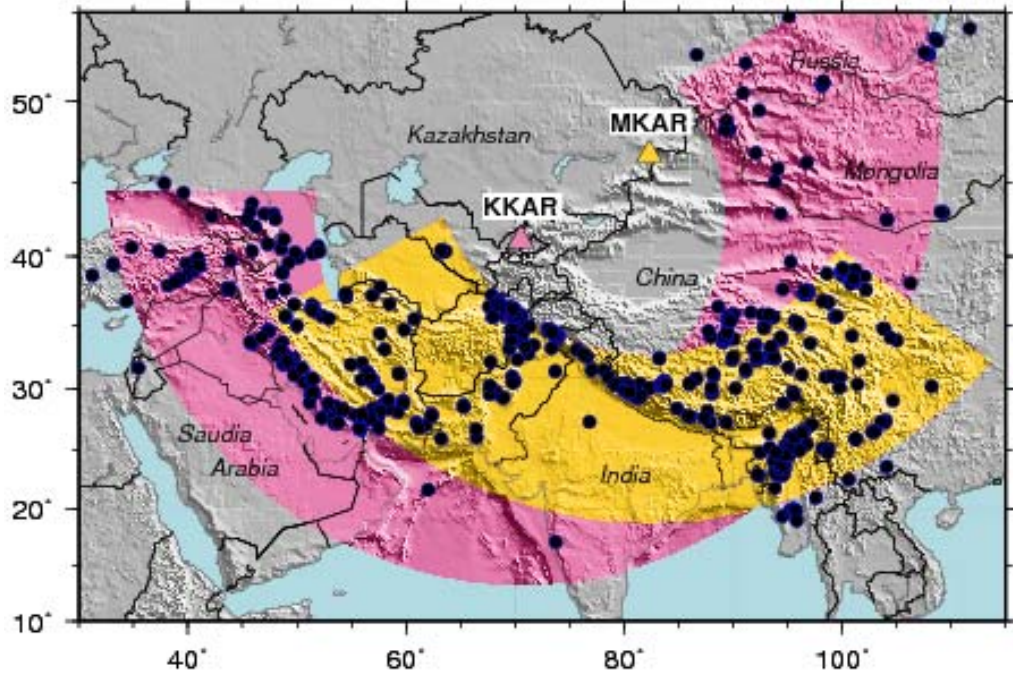


Figure 3. Map of south-central Asia showing the location of the Makanchi (MKAR) and Karatau (KKAR) arrays in Kazakhstan, as well as the location of ~500 earthquakes (circles) used in this study. Colored bands mark the 14 – 29° distance range from each array.

This report is organized in the following fashion: we first provide an in-depth description of the seismicity and tectonics that are observed in eight distinct zones at far-regional distances from the MKAR and KKAR arrays in Kazakhstan. Next, we describe the difficulties of far-regional phase analysis observed on the small apertures of the MKAR and KKAR arrays. In the fourth section of the report we show the results from our application of improved array signal-processing algorithms that are specifically designed for small-aperture arrays.

In the remainder of the report, we describe the methods we developed to better understand the path-specific structure that affects seismic body waves observed at far-regional distances from MKAR and KKAR. For example, in the fifth section of the report we used our array-processing results (slowness and phase-arrival times) to empirically derive regionalized velocity-depth profiles that more accurately predict the far-regional phase succession. These 1-D velocity-depth models are based on τ - p transformation of both array measurements and waveforms to form generalized representations of the path-specific earth structure.

In the sixth section of the report, we describe a waveform clustering algorithm that we devised to explain phase behaviors that are not predicted by the regionalized velocity-depth profiles. The clustering algorithm first sorts a set of array beams to derive 'wavefield templates'; i.e., grouped observations with similar phase characteristics. Then the wavefield templates are further analyzed in a non-linear fashion by comparing them with synthetic seismograms that are derived using the regionalized 1-D velocity-depth models.

In the final section, we describe two methods we used to examine near-array earth structure and its effects on array measurements. This involved the analysis of back-azimuth residuals from polarity studies, receiver functions to image below the arrays, and teleseismic *PcP* arrivals. In an appendix we demonstrate how small-aperture arrays such as MKAR and KKAR might be improved for far-regional phase analysis studies through the judicious use of sub-arrays or the addition of some carefully placed additional array elements.

This work has resulted in a methodology that improves the phase characterization of far-regional earthquakes observed on regional small-aperture array. Our research has also yielded insight into body-wave phases that are regularly observed on the MKAR and KKAR arrays, including information on expected wave propagation behavior and the regional nature of the upper-mantle discontinuities.

2. Far-Regional Seismicity Observed at the KKAR and MKAR Seismic Arrays

In the initial phase of the project we gathered relevant background information on the seismicity and tectonics at far-regional distances from the MKAR and KKAR arrays. Earthquakes occurring in these regions exhibit considerable complexity in the recorded seismograms, due to differences in source mechanism, earthquake depth, near-source structure, and upper-mantle discontinuity structure. Our specific goal was to regionalize the earthquake depths and source mechanisms, which gain insight into the phase behavior observed in our database of MKAR and KKAR waveforms. To facilitate this analysis we divided the seismic regions into separate zones of roughly similar tectonic regimes (shown in Figure 3), each of which we discuss in the following subsections.

2.1 Zone 1: Iran and Caspian

We derived our information on this zone of seismicity from several recent studies, including Tatar *et al.* (2004), Talebian and Jackson (2004), and Engdahl *et al.* (2006). Most of the seismicity in Iran results from the collision between Eurasian and Arabian plates, forming a 1000 km-wide zone of compression, which includes continent-continent collision and subduction (Figure 3). While the Zagros fold-and-thrust belt of SE Iran is the most seismically active region of Iran, it falls outside the 14 - 18° distance range we focused on during the project; thus, it was not included in our study. Following previous researchers, we divided the region labeled as Zone 1 in Figure 3 into the tectonic provinces shown in Figure 4. These provinces include 1) the Caspian Sea region including the Alborz and the Talesh range; 2) the Oman line and the Makran range; and 3) eastern Iran, which we discuss below.

The band of earthquakes that crosses the central Caspian Sea (Aphsheron-Balkhan sill) is thought to represent subduction of the South Caspian basin beneath the central Caspian (Jackson *et al.*, 2002). The south Caspian basin lacks seismicity and likely behaves as a rigid block. Earthquakes across the central Caspian occur to depths of 80 km, and there is little evidence that earthquakes shallower than 30 km occur on the offshore portion. Focal mechanisms (shown in

Figure 5) indicate normal faulting with the T-axis oriented N to NNE. Some strike-slip mechanisms have also been reported (Jackson *et al.*, 2002). On shore, shallower earthquakes occur (30 - 40 km), and focal mechanisms show thrust faulting. It is thought that the normal faulting earthquakes do not represent interaction of the Eurasian and Arabian plates, but rather plate bending and slab elongation from subduction.

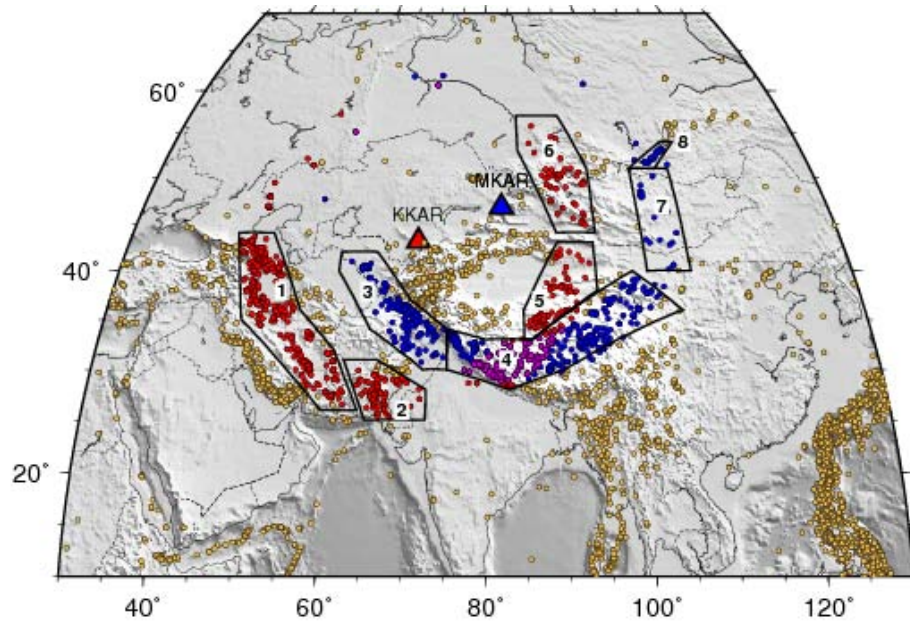


Figure 4: Far-regional seismicity (14 - 18°) from the KKAR (red circles) and MKAR (blue circles) arrays. Other seismicity is shown in yellow. The seismic zones discussed in the text are outlined and numbered. Epicenter locations are from the EHB catalog of Engdahl *et al.* (1998). Zone 1: Iran and Caspian, Zone 2: southern Pakistan, Zone 3: northern Pakistan and Afghanistan, Zone 4: Tibet, Zone 5: southern Tarim Basin, Zone 6: western Mongolia, Zone 7: central Mongolia, Zone 8: Southern Siberia.

Along the south Caspian Basin, earthquakes in the Alborz mountains occur shallower than 15 km, although events in the EHB catalog show depths of ~30 km. Most seismicity here exhibits left-lateral, strike-slip faulting or thrust faulting, with trends parallel to the regional strike. A few thrust mechanism strike perpendicular to the regional trend and may be associated with termination of strike-slip faults (Jackson *et al.* 2002). Overall, the mixture of strike-slip and thrust faulting likely accommodates the oblique left-lateral compression between central Iran and the southern Caspian.

The west coast of the Caspian includes the N-S trending Talesh range, a continuation of the Alborz. Seismicity here is deeper than along the Alborz, ranging between 15 - 26 km depth. Focal mechanisms for these earthquakes (see Figure 5) indicate very shallow angle thrust faults (near horizontal), with slip vectors oriented to the west.

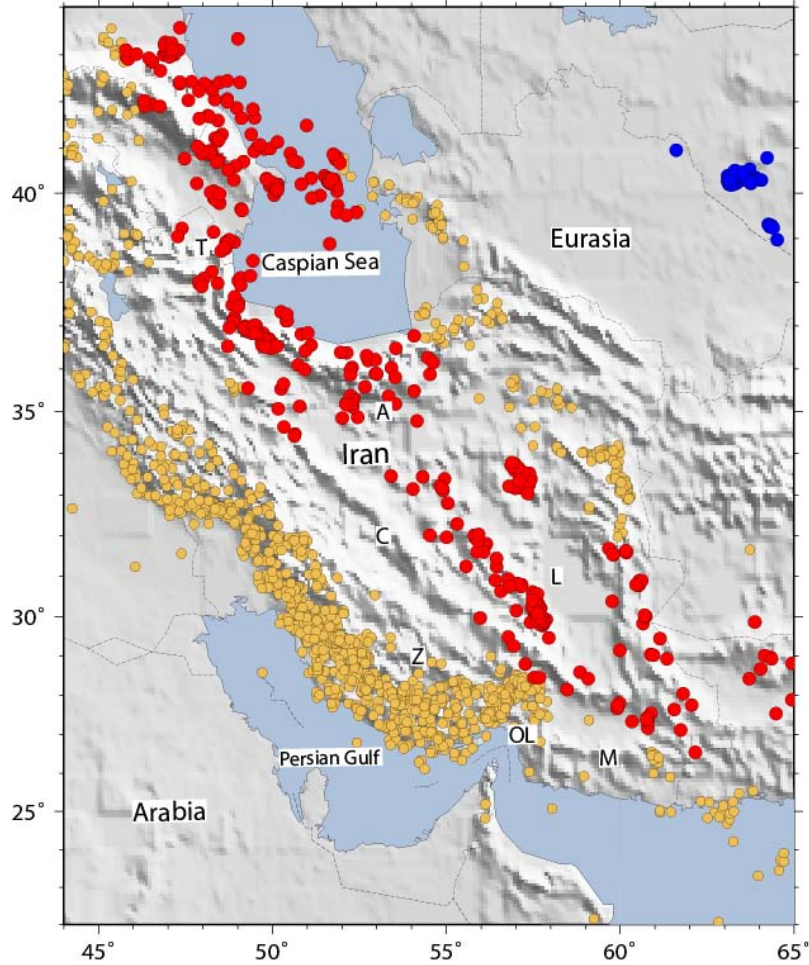


Figure 5: Seismicity in Iran and the Caspian Sea region (from Engdahl *et al.*, 1998). Red circles are earthquakes observed at 14 - 18° from KKAR array. Gold circles show the seismicity of the Zagros and other earthquakes of the region. Localities mentioned in the text are labeled as follows: Zagros (Z), Oman line (OL), Makran (M), Lut block (L), Central Iran block (C), Alborz (A), and Talesh (T).

The Oman line marks the transition between the Zagros continent-continent collision and the subduction of the Arabian plate beneath the Makran coast. A change in earthquake depth is observed from the shallow upper crustal seismicity of the Zagros (< 20 km) to the subcrustal seismicity in the Makran region. Earthquakes deepen northward, ranging from 8 - 12 km near the coast to a depth of 28 km just 50 km to the north. Most focal mechanisms show thrust faulting, although some strike-slip mechanisms appear in the Harvard CMT catalog (Figure 5). In the Makran region, seismicity is seen throughout the crust and extends into the upper mantle to depths greater than 50 km (Maggi *et al.*, 2000). This deeper seismicity likely occurs on the down-dip portion of the subducting Arabian plate. Focal mechanisms for the deeper seismicity show normal faulting with T-axis oriented to the north and some N-S strike-slip faulting.

In eastern Iran most seismicity occurs along the boundaries of the Lut and central Iranian continental blocks, which are relatively stable and aseismic. This region has historically produced large and devastating earthquakes (e.g., Tatar *et al.*, 2004). Earthquakes occur mostly in the upper

crust above 20 km depth. The EHB catalog shows a mean depth of 12 ± 5 km (Engdahl *et al.*, 2006). On the western edge of the Lut block, the focal mechanisms shown in Figure 5 indicate predominantly NNE-SSE strike-slip faulting. These faults likely accommodate the right-lateral shear between central Iran and Afghanistan to the west. On the eastern boundary of the Lut block, a NNW-striking thrust fault appear to be the dominant mechanism; however, strike-slip faults are also apparent in the Harvard CMT catalog.

We also compiled information regarding the crustal structure across the region. Most of this information is extracted from the CRUST2.0 model (Bassin *et al.*, 2000). Some information is also gathered from receiver function studies (e.g., Mangino and Priestley, 1998). The various regions show large variation in crustal thickness. Across the southern Caspian basin the crust ranges from 30 to over 45 km thick, with the thickest crust onshore. Across the Zagros to central Iran, the crustal thickness increases from 45 km thick to over 70 km thick, showing an abrupt increase east of the main Zagros thrust (Paul *et al.*, 2006). Profiles extracted from CRUST2.0 indicate a variation of 31 – 39 km in crustal thickness.

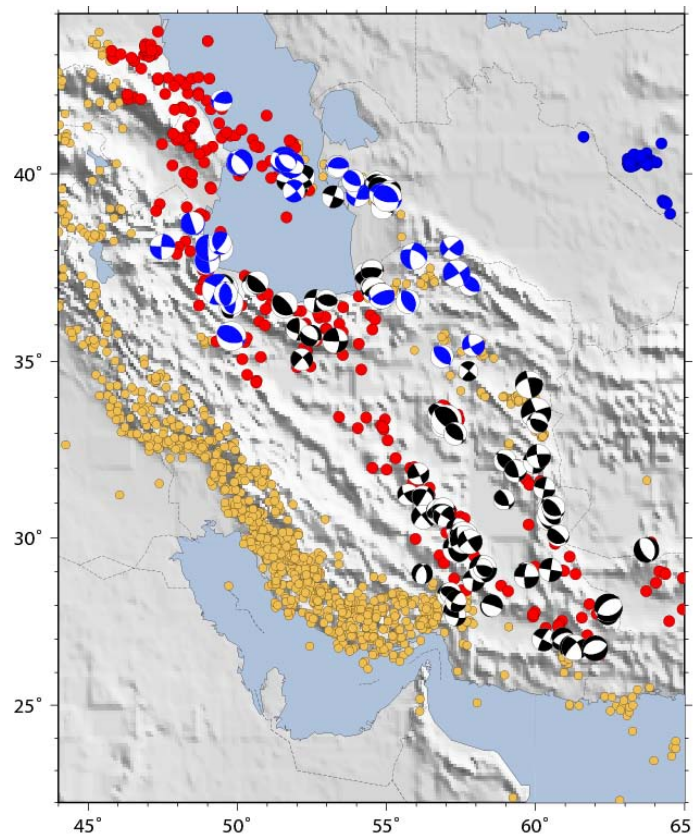


Figure 6: Focal mechanism for Iran and the Caspian Sea region discussed in the text. Compressional quadrants are darkened. The best double-couple Harvard CMT solutions are shown in black. Blue mechanisms are from Jackson *et al.* (2002) for the Caspian region. Mechanisms for the Zagros are not shown.

2.2 Zone 2: Southern Pakistan

Seismicity in southern Pakistan (Figure 6, left) is at far-regional distances ($14 - 18^\circ$) from the KKR array. Most information presented here is summarized from Quittmeyer and Jacob (1979) and Ambraseys and Bilham (2003). The majority of earthquakes in southern Pakistan result from the convergence between the Eurasian and India plate. In Pakistan, high seismicity is observed along the Kirthar and Sulaiman fold-and-thrust belts, which form the western boundary of the collision. Seismicity also occurs along the Makran mountain range, along the south coast. Earthquakes in the Sulaiman range fall outside of the far-regional distance focus of this study and were not part of our analysis.

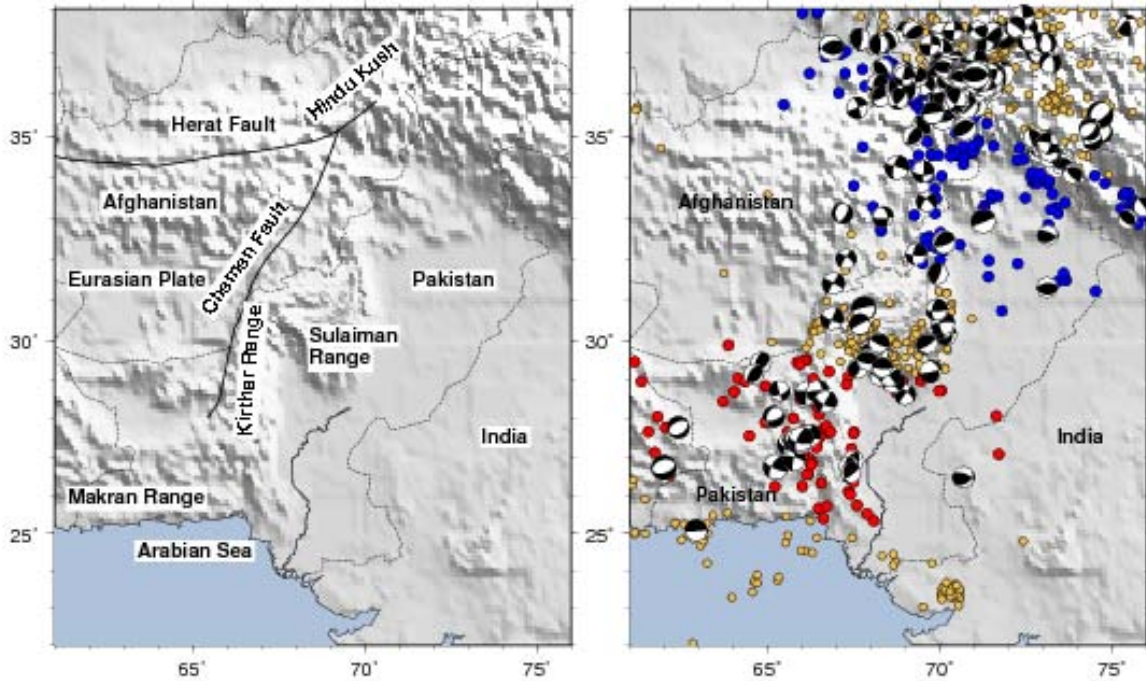


Figure 7. Left: Reference map of Pakistan and Afghanistan with places discussed in the text labeled. Right: Map showing regional seismicity, red and blue circles are at far-regional distances from KKR and MKAR, respectively. Gold circles show other regional seismicity. Focal mechanism are the best-double couple solution from the Harvard CMT catalog.

The Kirthar range is bounded on the west by the Chaman fault, a 1000-km long left-lateral fault system that likely marks the boundary between the Indian plate to the east and the Eurasian plate (Ambraseys and Bilham, 2003). From the Harvard CMT catalog, focal mechanisms show strike-slip, thrust and normal faulting within the Kirthar region (Figure 6, right). The normal faulting events occur at depths greater than 50 km and may be related to the subduction of the Arabian plate beneath the Makran coast. In general, earthquakes with well-determined depths occur above 30 km, at an average depth of 18 km, similar to other continental regions. The shallower earthquakes show left-lateral mechanisms that strike NNE-SSW and thrust faulting with

the T-axis oriented NW, consistent with strain partitioning due to oblique convergence between the Indian and Eurasian plates.

We have not been able to find peer-reviewed studies of the local crustal structure (e.g., receiver functions). However, the CRUST2.0 model (Bassin *et al.*, 2000) shows a trend of crustal thickening from the Makran coast north into the Kirthar range, where the thickness of the crust is on the order of 45 km.

2.3 Zone 3: Northern Pakistan and Afghanistan

Earthquakes in this zone are at far-regional distances from the MKAR array (Figure 7). The region includes the western Himalayan syntaxis beginning in northern Pakistan and extends through the Pamir Hindu Kush region of Afghanistan. Seismicity in Tajikistan and Uzbekistan are also included in this zone. The main structural features trend northwest-southeast, and most seismicity is associated with Indian and Eurasian collisional plate boundary.

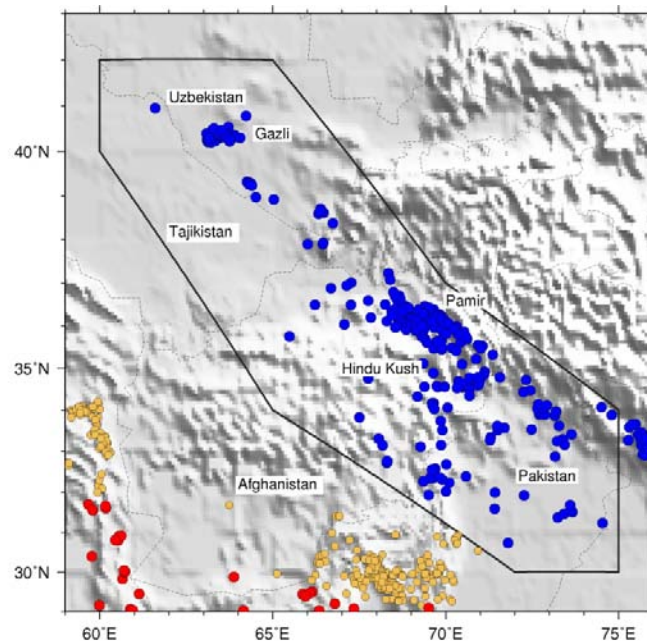


Figure 8. Seismicity in northern Pakistan, Pamir Hindu Kush and Uzbekistan (from Engdahl *et al.*, 1998). Blue circles are earthquakes observed at far-regional distances from the MKAR array.

In northern Pakistan the main seismic zone trends northwest following the trend of the Himalayas. Source mechanisms show mostly thrust fault motion with NW-SE oriented fault planes. Some strike-slip mechanisms are also observed. The earthquakes tend to have shallow focus (confined to the mid-and-upper crust) and most are associated with the northward dipping fault system that separates the India plate from the Eurasian plate. Receiver function studies (Zugibe *et al.*, 2008) indicate that the crust in this region is on the order of 60 km thick along the Himalayan front.

The Pamir Hindu Kush seismic zone is an active region of intermediate depth earthquakes and has seismicity that extends to 300 km depth (Searle *et al.*, 2001). The mountain ranges are relatively old and are thought to have been reactivated during the Indian-Eurasian collision. The convergence of the Pamir range with Eurasia also causes shallow focus earthquakes (< 45 km) along the thrust fault system between the two plates. The Hindu Kush seismic zone is bounded on the east by the Chaman left-lateral fault system (Figure 8) and on the west by the right-lateral Karakorum fault (Searle *et al.*, 2001).

The pattern of seismicity in the Pamir Hindu Kush seismic zone is quite complicated at depth (Billington *et al.*, 1977; Roecker, 1982). A large scale relocation study (6000 events; Pegler and Das, 1998) indicates that this seismic zone has an S-shaped pattern. At depth, the earthquakes map a 700-km long zone that is 30 km wide, which potentially represents thin subducted continental crust. It has been hypothesized that the northward dipping seismic zone occurs on Indian lithosphere subducting beneath the Hindu Kush, and the southward dipping seismicity occurs on Asian lithosphere underthrusting the Pamir range (Burtman and Molnar, 1993).

North of the Pamir Hindu Kush, seismicity in the Tajikistan/Uzbekistan region occurs in an intraplate setting, where earthquakes are occurring in Asian lithosphere. Strain in the region is associated with the Indian and Eurasian collision and many thrust faults exist, although strike-slip also occur. Most earthquakes show thrust mechanisms with various fault plane orientations. A study of the Gazli region of Uzbekistan, where magnitude 7 earthquakes have occurred, indicates that most earthquakes occur above 25 km, likely marking the limit of the brittle ductile transition.

2.4 Zone 4: Tibet

The Tibetan plateau forms a high topography region with an elevation of 4 - 5 km above sea level and is underlain by ~70 km thick crust. Earthquakes in Zone 4 are observed by both MKAR and KKAR at far-regional distance, with some overlap between the arrays. Most seismicity is located in the Lhasa Block (Figure 8), one of the several old suture zones that have undergone north-south shortening and east-west extrusion to form the high topography and accommodate strain. It is suggested that the entire plateau is underlain by cold lithospheric mantle (Priestley *et al.*, 2006), however the extent that the Indian plate subducts beneath the plateau is still debated (e.g., Curtis and Woodhouse, 1997; Zhou and Murphy, 2005). Low upper-mantle S velocities beneath the central and northern plateau, inefficient S_n propagation and slow P_n velocities are also reported (e.g., Barazangi and Ni, 1982; McNamara *et al.*, 1997).

Most seismicity across the plateau occurs at shallow depths (< 25 km), and deeper earthquakes tend to be poorly constrained (Langin *et al.*, 2003). The shallow earthquake depth may be indicative of a hot upper mantle below the plateau, creating a shallow brittle/ductile transition. A seismicity study from the INDEPTH III experiment (Langin *et al.*, 2003), shows that earthquakes predominantly exhibit both normal and strike slip faulting mechanisms. However, some do exhibit thrust mechanisms. Fault plane solutions are consistent with shortening in the north-south direction, as well as extension in the east-west direction.

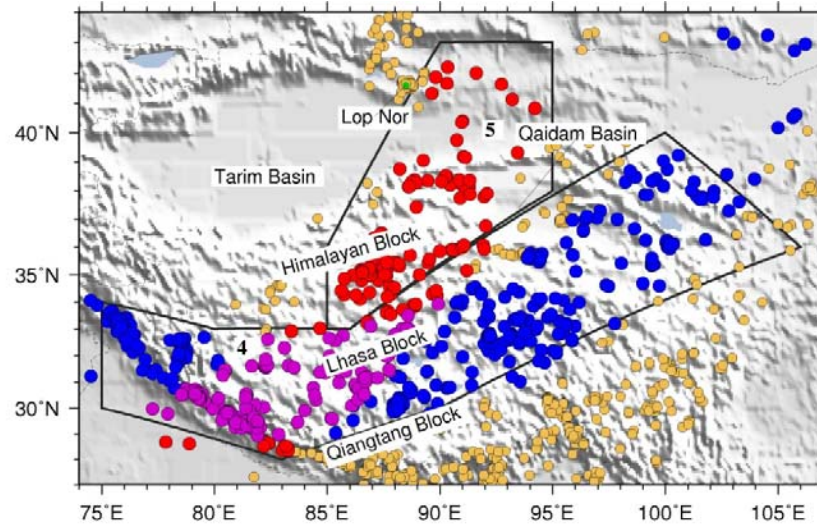


Figure 9. Zone 4 and Zone 5. Red circles are earthquakes observed at far-regional distance by the KKAR array, blue circle are observed by the MKAR array, purple circles are observed by both arrays. Gold circles are earthquakes outside the far-regional range from these two arrays. The major suture zones across the plateau are labeled. The Chinese Lop Nor test site is also labeled (green circle).

2.5 Zone 5: Eastern Tarim Basin

This zone includes earthquakes observed by the KKAR array at far-regional distances (Figure 8). It includes part of the Himalayan Block of the Tibetan Plateau and the eastern edge of the Tarim basin, as well as part of the Qaidam basin. The Chinese Lop Nor nuclear test site sits to the north of the zone. A large left-lateral fault system (Altyn Tagh) separates the Tibetan Plateau from the Tarim basin in this region (Hetzl *et al.*, 2004). Across the basins to the plateau crustal thickness varies from 48-70 km (Leech *et al.*, 2010). Most earthquakes have focal depths above 35 km, with a few extending deeper. Focal mechanisms in this zone show both left-lateral strike slip motion (along the boundary between the Tarim basin and the Tibetan Plateau) and thrust faulting on the Tibetan Plateau.

2.6 Zone 6: Western Mongolia

Seismicity in western Mongolia occurs along the Altay Mountains (Figure 9). It is recorded at far-regional distances by the KKAR array. The active tectonics of Mongolia results from the collision of the Indian and Eurasian plates. Most of the active faulting and seismicity occurs in the Western portion of Mongolia along the Altay Mountains. Within the linear mountain belt are parallel, right-lateral strike-slip faults and some E-W thrust faults. The faulting is thought to accommodate shortening between western China and Siberia (Walker *et al.*, 2006).

According to Bayasgalan *et al.* (2005), all earthquakes in Mongolia have centroid depths shallower than 20 km. In the Altay Mountains, focal mechanisms are consistent with right-lateral strike-slip faulting on NW-SE oriented faults. Thrust mechanisms occur on E-W faults. The pattern of faulting might accommodate vertical axis rotation around fault bounded blocks (Baljinnyam *et al.*, 1993). Seismic studies of the crustal structure of western and central Mongolia have not been yet published. Results from a 2003 seismic deployment across Mongolia and the Baikal region are currently in press. Most information concerning the crustal structure comes from petrologic and thermobarometric studies of young xenoliths and also gravity modeling (e.g., Petit *et al.*, 2002). These studies suggest that the crust is 46 km under the Altay Mountains.

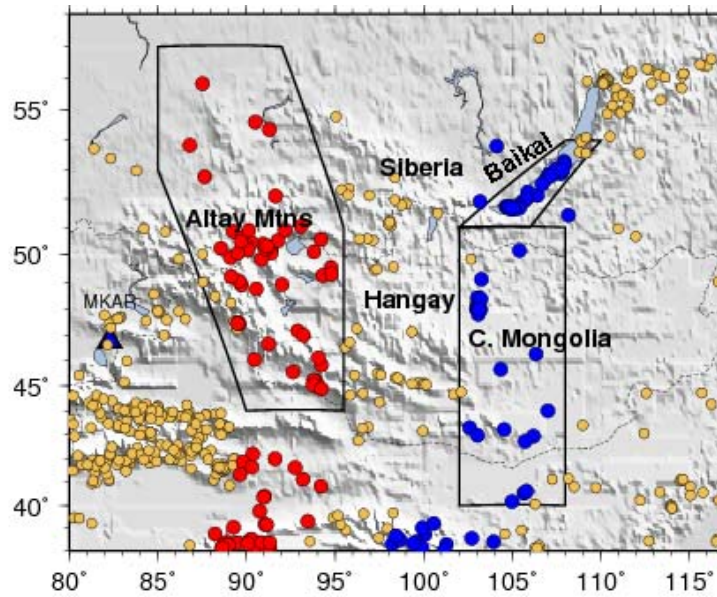


Figure 10. Map of regional seismicity for Mongolia and the Baikal Rift Zone. Earthquakes at far-regional distance from KKAR (14 – 18°) are shown in red and from MKAR in blue. Other seismicity is denoted with gold circles. Labels indicate places discussed in the text.

2.7 Zone 7: Central Mongolia

There is less seismicity in central Mongolia compared to the Altay Mountains of western Mongolia. The earthquakes in central Mongolia are observed by the MKAR array at far-regional distances. They occur on the eastern edge of the Hangay region, a Proterozoic continental block that is bounded on the east by a large right-lateral strike-slip fault system. The Hangay region forms a topographic dome and is mostly aseismic, although normal faulting events do occur on its northern edge. The crust beneath the Hangay has a maximum depth of 50 ± 3 km (Petit *et al.*, 2002). Most earthquakes in the region occur shallower than 20 km (Bayasgalan *et al.*, 2005). Focal mechanism show right-lateral strike slip faulting along north-south fault orientations, consistent with the local tectonics.

2.8 Zone 8: Baikal Rift Zone

The Baikal rift forms an 1800-km depression in southern Siberia. It has been one of the most seismically active rifts on the planet for more than the last 30 Ma, but only exhibits 10 – 20 km of overall extension (0.3 – 0.6 mm/yr). Geodetic rates indicate much faster extension rates on the order of 1 mm/yr (Suvorov *et al.*, 2002). Seismicity here is recorded by the MKAR array at far-regional distances (14 – 18°).

Numerous studies have examined the crustal structure of the rift and surrounding region (e.g., Gao *et al.*, 2004; Brazier & Nyblade, 2003; ten Brink & Taylor, 2002; Suvorov *et al.*, 2002; Bayasgalan *et al.*, 2005; Emmerson *et al.*, 2006). Receiver function profiles reveal a crust that ranges in thickness from 37 – 45 km (Gao *et al.*, 2004). The thickest crust is found to the north under the Siberian platform and south below the Mongolian fold and thrust belt. The thinnest crust is below the central portion of the Baikal rift, where the crust is 35 km thick. Upper mantle seismic velocities show a 2 – 5% slow anomaly below the rift axis, likely due to increased temperature from extension related mantle upwelling. The crust within the rift and surrounding region has an average *P* velocity of 6.4 km/s (Suvorov *et al.*, 2002). A detailed seismic study of the rift (ten Brink & Taylor, 2002) shows up to 4 km of slow sediments (1 – 3 km/s) underlain by 20 km of with typical continental velocities (5 – 6.5 km/s) and 10 km of relatively fast lower crust (7 – 7.4 km/s).

Earthquakes in this region are mostly associated with extension and show predominantly high-angle normal faults, with the *P* axis oriented to the NNW. Some strike-slip faulting is also observed (Emmerson *et al.*, 2006). In the western portion of the rift, earthquakes occur above 16 km depth, but earthquakes of up to 30 km depth are seen in the NE rift portion.

3. Phase Characterization Using Small-Aperture Regional Arrays

The regional seismic arrays of the International Monitoring System (IMS) should be a rich data source for the study of far-regional phase behavior, since they are all comprised of high-quality borehole seismometers that record high-fidelity signals. However, beyond regional distances, the small apertures (< 5 km) and spatial configurations of these arrays limit their usefulness beyond *P* and *S* first-arrival onset picks. Standard array methods (e.g., slant stacking and frequency-wavenumber analysis) cannot resolve the azimuths and slownesses of primary and secondary arrivals, making confident arrival identification and classification difficult.

The main function of a seismic array is to improve signal-to-noise ratio through stacking and to measure arrival times and directional parameters from the beam-forming process. The performance of a particular array depends on many factors, including site noise levels, signal coherence and the array geometry. For optimal performance an array's geometry (aperture and inter-station spacing) should be tuned to the characteristics (e.g., frequency, phase velocity, and direction) of the signals of interest. Array geometry tuning is typically a balancing act to adequately address optimal cross-array signal coherence, spatial aliasing, measurement resolution, as well as the local noise characteristics. The trade-offs between array aperture and inter-sensor spacing can be generalized in several ways. First, larger array apertures imply a longer

triangulation arm, which allows for more confident back-azimuth estimates. A larger aperture also decreases the likelihood that the local noise field will be coherent across the array, thereby improving signal gain levels achieved by stacking. Arrays with larger apertures also produce more precise measurement of signals with high phase velocities (steep incident angles), because the travel time across the array is increased. Conversely, if the array aperture is too large, structural heterogeneity across the array and other site effects can negatively impact signal coherence between array elements and degrade array stacking performance. Finally, large inter-sensor spacing also increases the possibility of wavenumber aliasing, since the spatial Nyquist frequency is related to the maximum sensor separation distance. Wavenumber aliasing increases the uncertainty associated with measurements of multiple arrivals within an analysis window.

The expected phase velocities of far-regional P arrivals (e.g., P_n , P_{410} , P_{660} , and depth phases) range between 8 - 12.5 km/s, using the AK135 reference model (Kennett *et al.*, 1995). Most signal energy occurs in the 1 to 4 Hz band, based on spectral analysis of our far-regional dataset at MKAR and KKAR. This indicates that incoming signals have wavelengths of 2 – 10 km with corresponding spatial frequencies of 0.5 to 0.1 (units of 1/km which is equivalent to the wavenumber/ 2π). This is illustrated in Figure 10, where we show the relationship between temporal frequency and spatial frequency for the expected range of far-regional phase velocities. Spatial frequency is important for understanding an array's response.

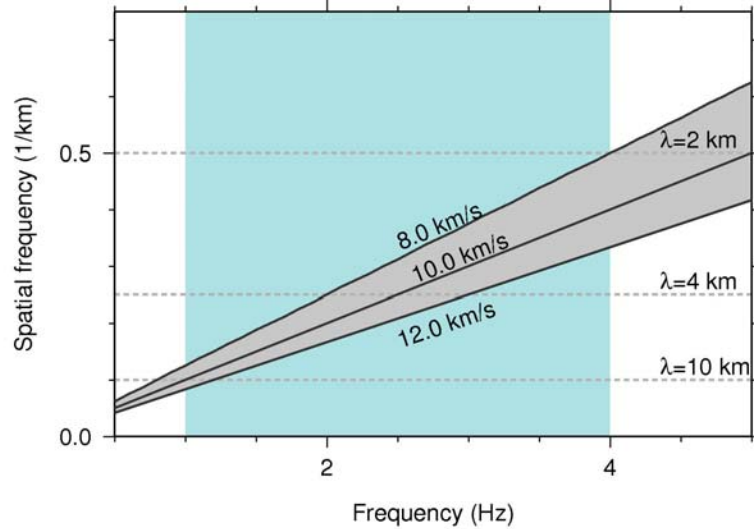


Figure 11. Temporal frequency versus spatial frequency for the expected range of far-regional phase velocities. The blue region highlights the main frequency band of our far-regional observations. The grey region marks the far-regional spatial/temporal frequency bands, which is of interest to this study.

The nine-element borehole arrays at MKAR and KKAR have similar designs (Figures 11 and 12): both contain an outer ring of five elements, an inner ring of three elements, and one central element. The maximum aperture at MKAR depends on the direction of the incoming signal. For signals from the southwest/northeast the effective aperture is ~3 km and for signals from the northwest/southeast the effective aperture is ~5 km. The non-symmetrical nature of the MKAR

array indicates that its performance varies depending on the direction of the incoming signal. In other words, analysis of signals from the northwest/southeast recorded at MKAR will be potentially better resolved in azimuth due to the larger effective array aperture, and hence larger triangulation arm. The KKAR array is more symmetric and has an effective aperture of 3 – 4 km, depending on the direction of the incoming signal.

Examination of the frequency-wavenumber array response functions for both arrays (Figures 11 and 12) shows that the arrays are not optimally designed for full slowness and back-azimuth resolution at far-regional distances, especially when considering multiple *P* arrivals within a 5 – 20 second analysis window. The main lobe of the response functions has a 50% reduction of power at the spatial frequency of 0.15 (1/km) at MKAR and 0.2 (1/km) at KKAR. A simple rule of thumb states that the sharper the main lobe, the more precise the slowness measurements. Thus, at the temporal frequencies of interest (1 – 4 Hz), the precision of slowness/azimuth measurements at MKAR and KKAR can be negatively affected, and multiple signal arrivals can become difficult to discern with any confidence, especially when they have similar slowness values.

For example, in the AK135 reference model, an event observed at 15° epicentral distance has a predicted *P*_n arrival velocity of 8.15 km/s and a *P*₄₁₀ arrival velocity of 10.0 km/s. These correspond to spatial frequencies at 2 Hz of 0.25 (1/km) and 0.2 (1/km), respectively. Since the main lobe of the MKAR response function has a half-width of 0.15, the similar arrival parameters might smear the phases together, at least for spectral array-processing methods that do not retain arrival-time information. At higher spatial frequencies (shorter wavelengths) the array response functions exhibit aliasing lobes. Optimal array response functions have low-amplitude side lobes and a sharply peaked main lobe. However, at MKAR an aliasing lobe at 50% power occurs at spatial frequencies of ~0.45 (1/km) and at KKAR they appear near 0.5 (1/km). Aliasing lobes can also make it extremely difficult to accurately identify multiple arrivals, because the high gain of the side lobes can amplify nuisance signals, which can then be misinterpreted. While frequency-wavenumber response functions (as shown here) are most directly applicable to spectral array processing methods, such as the Capon method (Capon, 1969), in time-domain array methods (e.g., Nth root and phase-coherence semblance stack), the effects of the broad main peak and side lobes manifest as smearing in the slowness and azimuth vespagrams, which also reduces measurement precision. We will demonstrate this effect in the next section of the report.

In summary, the configurations of the MKAR and KKAR arrays are not optimally designed for analyzing the far-regional *P* arrival suite. The primary difficulty we have encountered is the small array aperture, which limits the precision in the arrival measurements for the range of far-regional phase velocities and frequencies when analyzed with common array methods. The lack of precision makes confident phase identification difficult, since multiple arrivals with similar propagation parameters occur within a 5 – 20 second arrival window. To mitigate these limitations, we present a modified array processing scheme in the next section (phase-weighted semblance stacking) that overcomes some of these issues. Conversely, we note that, in general, the configuration of the MKAR and KKAR arrays performs well in regional waveform analysis or for first-arrival onset picking of teleseismic phases, where straight stacking to reduce noise is the primary objective.

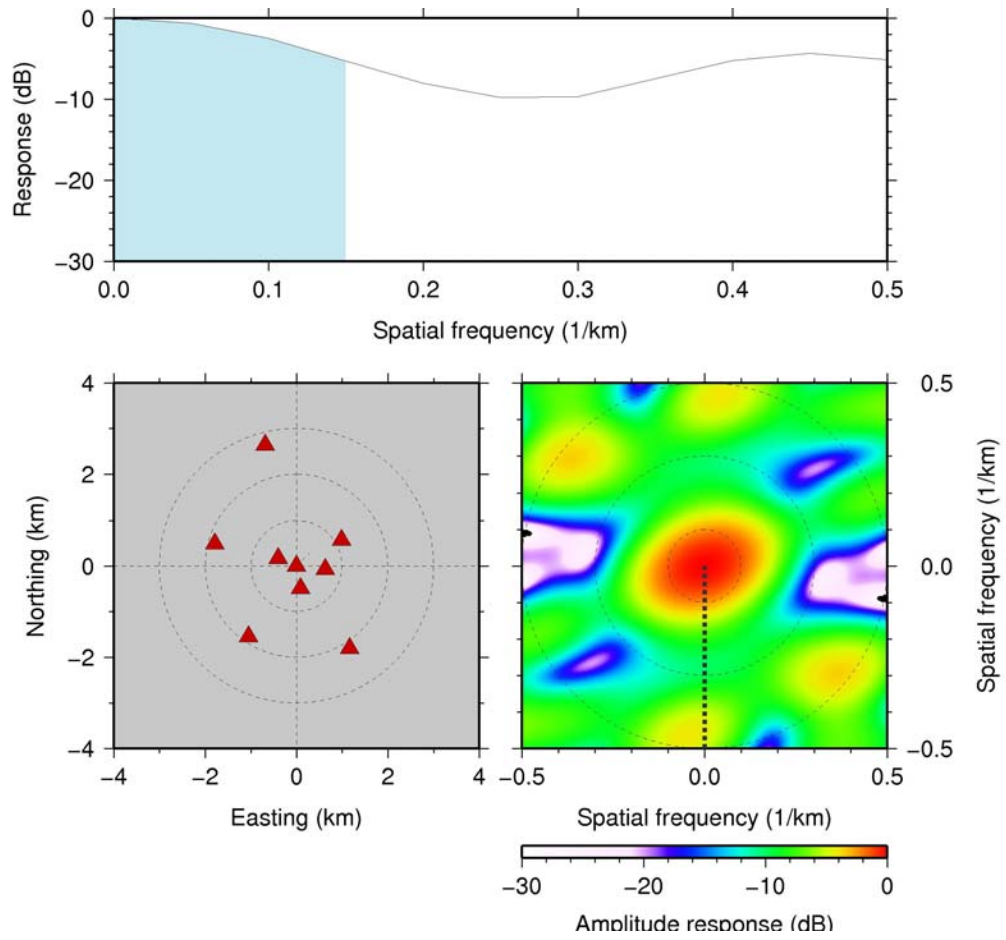


Figure 12. MKAR array response function. *Top:* Cross section through response function, showing the spatial frequency at which the amplitude gain is at 50% power loss and the aliasing lobe near 0.45 (1/km). *Bottom Left:* MKAR array configuration; *Bottom Right:* MKAR response function. All amplitudes are shown as normalized decibels.

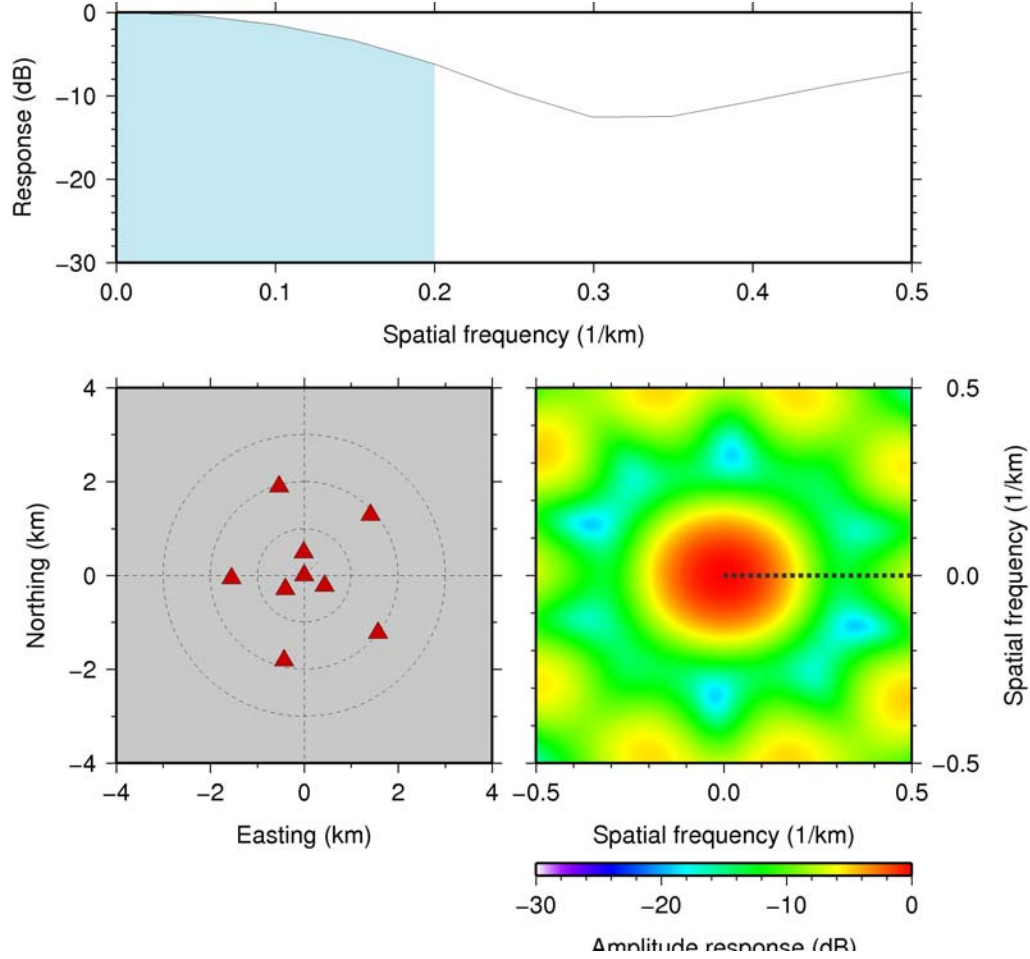


Figure 13. KKAR array response function. *Top:* Cross section through response function, showing the spatial frequency at which the amplitude gain is at 50% power loss and the aliasing lobe near 0.45 (1/km). *Bottom Left:* KKAR array configuration; *Bottom Right:* KKAR response function. All amplitudes are shown as normalized decibels.

4. Phase-Weighted Semblance Stacking of Small-Aperture Array Observations

Over the course of this effort we have investigated various beamforming methods and their ability to improve the analysis of far-regional arrivals recorded by small-aperture arrays. The investigation included both spectral frequency-wave number methods (e.g., Capon, 1969), multiple signal characteristic (MUSIC; Stoica and Nehorai, 1989), cross-correlation (Tibuleac and Herrin, 1997), and other slant-stack beamforming methods (e.g., N^{th} Root, see Rost and Thomas, 2002).

While frequency-wave number methods (e.g., Capon) can perform well at measuring arrival slowness and back-azimuth, they perform poorly in the case of multiple signal arrivals within a single analysis window. The loss of arrival-time information on the individual arrivals, due to the spectral formulation, makes unraveling the P-arrival suite nearly impossible. At far-regional distances multi-pathed arrivals commonly interfere with each other (constructively and destructively) and exhibit similar arrival slowness over the 5 – 20 second duration of the main P-wavetrain. Accurate arrival-time information is crucial in sorting the phase arrival progression

in such scenarios. Windowing the arrivals using a Short-Time-Fourier-Transform method is an option; however, arrival-time resolution is still problematic due to close arrival spacing, and choosing optimal analysis windows is difficult without affecting the quality of the Fourier Transform. In general, arrival-time resolution is an issue for most moving-window type analysis schemes, including slant-stack Nth-root and cross-correlation implementations. Methods such as MUSIC do not suffer these limitations and can perform well on far-regional arrivals; however, one major drawback of this method is the need to know *a priori* how many arrivals are in the analysis window. In many cases, emergent first arrivals and weak secondary arrivals can be easily missed without high-level scrutiny by an analyst.

For the far-regional phase identification problem, an optimal beamforming method needs to enhance weak arrivals and be unbiased in amplitude and phase, so that large amplitude arrivals do not obscure smaller amplitude arrivals. The method should also be able to simultaneously determine slowness and back azimuth, while preserving the phase arrival time. We have developed a processing technique that comes close to meeting these criteria, which we call phase-coherence semblance stacking (PCSS). This technique has the signal-to-noise increasing power typical of slant-stack methods, but through the incorporation of both a phase coherency measure and amplitude semblance, it produces a measure that is highly sensitive to signal onset time and overcomes some of the slowness and azimuth resolution limitations of small-aperture arrays. The technique's sensitivity to onset time also holds for very emergent arrivals.

In our implementation, both instantaneous phase coherence and semblance are simultaneously determined for a range of slowness and back-azimuth combinations (i.e., vector slownesses), resulting in a 3-dimensional (3-D) phase-coherence semblance function (time, slowness, back azimuth). Phase coherence and semblance are combined through a linear mixing, and the two coherency measures are complementary. Instantaneous phase coherence is an unbiased amplitude measure that is maximized for the vector slowness that aligns the signals most closely in the complex plane. Semblance is maximized for vector slownesses at which the total beam power equals the average beam power over all traces, thus favoring high-amplitude correlation and high signal-to-noise ratios.

Instantaneous phase is a feature of complex signal analysis, in which the angular phase can be described for each sample point in the time domain through a linear transformation. To determine the instantaneous phase, we transform each seismic trace $s(t)$ for station j into its complex representation, $X_j(t)$, by combining the real trace with its Hilbert transform, such that

$$X_j(t) = s_j(t) + iH[s_j(t)].$$

On the right side, the term i denotes the imaginary unit and $H[s_j(t)]$ is the Hilbert transform for each seismic trace j . To equalize the power at each sample point and to limit $X_j(t)$ to the unit circle in the complex plane, we normalize by the magnitude of $X_j(t)$,

$$X_j(t) = \frac{s_j(t) + iH[s_j(t)]}{|s_j(t) + iH[s_j(t)]|}.$$

This limits the magnitude of $X_j(t)$ to values between 0 and 1. For our purposes, it is more convenient to rewrite $X_j(t)$ using Euler's formula,

$$X_j(t) = A_j(t) \exp [i\phi_j(t)],$$

where each complex trace is separated into its amplitude envelope function, $A(t)$, and instantaneous phase component, $\phi(t)$. Since we are interested in optimal beamforming, we determine the phase coherence between all seismic traces by computing an instantaneous phase stack for a range of vector slownesses θ_i , such that the phase stack, c , for each time sample and for vector slowness i , is written as

$$c_i(\theta_i, t) = \frac{1}{M} \sum_{j=1}^M \exp [i\theta_i (t + T(r_j, \theta_i))]^\gamma.$$

Here the term $T(r_j, \theta_i)$ is a time delay that depends on the array element position vector $r_j(x_k, y_k)$ and slowness vector θ_i . Since we are averaging the instantaneous phase over all seismic traces ($j = 1, 2, 3 \dots M$), the phase stack, $c_i(\theta_i, t)$, has a value between 0 and 1, where 0 means the traces are completely out of phase for that sample point and slowness vector, and 1 means the traces are completely in phase and thus perfectly coherent. The sharpness of the phase stack can be controlled by the exponent γ , which can have a value > 1 . High values can be useful for cases of low signal-to-noise on some array elements, and we have typically used values of 2 or 3. In some cases it is also useful to average the phase stack over a time gate of time samples m , using

$$\bar{c}_i(\theta_i, t_{(n+m/2)}) = \frac{1}{m} \sum_{t=t_n}^{t_{n+m}} c_i(\theta_i, t).$$

This is particularly useful to smooth the phase stack function and in the calculation of statistics (e.g., the F-statistic). In our analysis we found that time gates of 5 to 10 samples produced good results.

A similar, but less complete description of the instantaneous phase stack can be found in Schimmel and Paulssen (1997). However, in their implementation, they found it useful to weight each sample of the linear beam by the phase stack at each sample point. Thus, in their implementation, vespagrams would be constructed by weighting the beam trace with the phase stack. In contrast, we have found it more beneficial to directly use the phase stack, $c(t)$. This permits a clearer picture of the arrival structure, since it does not obscure small amplitude arrivals, and allows a better measurement of signal onset time. The phase coherence values also lend themselves to more straightforward uncertainty assessment, since a coherence value of zero indicates that the signals are completely out of phase for a particular time, slowness, and back azimuth, while a value of one indicates they are completely in phase. The difference between the two vespagram analysis methods is illustrated in Figure 13 for a typical far-regional event with emergent first arrivals recorded by the MKAR array (Table 1).

Table 1. ISC location for the event shown in Figures 13, 14, and 15.

| Date | Origin Time | Latitude (°) | Longitude (°) | Depth (km) | m_b | Region |
|------------|-------------|--------------|---------------|------------|-------|----------|
| 10/27/2006 | 07:55:02 | 29.88 | 80.04 | 10 | 4.2 | N. India |

Figure 13 shows that the vespagrams constructed from weighted beam power are dominated by the largest amplitude signals in the record. While the emergent first arrivals are still apparent (between 0 – 2 seconds in Figure 13), they appear significantly less energetic in the vespagram than the dominant signals, which appear near the 6- and 10-second marks and could easily be missed in a noisier record. However, the vespagram slices representing the phase stack (i.e. phase coherence) values clearly delineate the emergent first arrivals at the same coherence level as the larger amplitude signals. It is this aspect of the phase-coherence method that makes it particularly useful for analyzing far-regional coda arrivals.

Also apparent in Figure 13 is the limitation in slowness resolution of small-aperture arrays. While phase-coherence processing is an improvement over other slant-stacking methods, significant slowness smearing still occurs, which increases uncertainty in phase identification. This issue is slightly improved by including the semblance calculation (shown below), but is a function of the limited array aperture. It is possible that further improvement will only be realized by increasing the aperture of the arrays and inter-station spacing; for instance, by installing an outer ring on regional arrays.

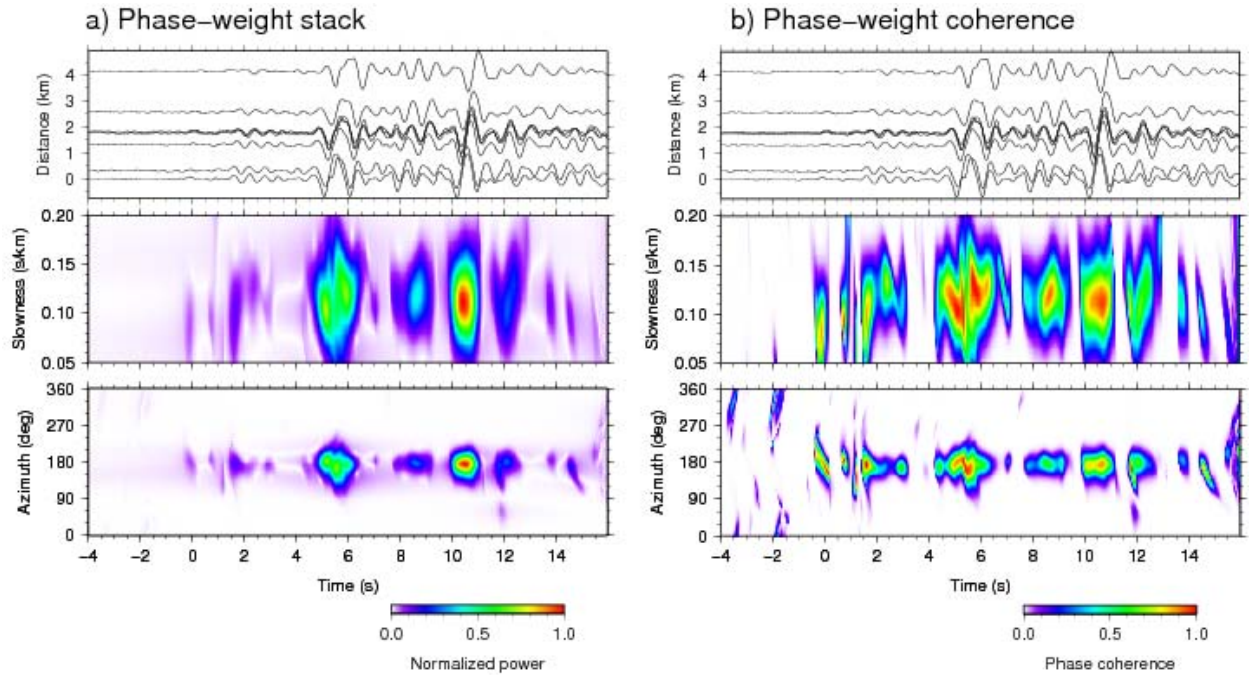


Figure 14. Slowness and back-azimuth slices through 3-D vespagrams from (a) phase-weighted beams and (b) phase-weighted coherence values. The top panels show the array gathers, the middle panels show a slowness slice along for a constant back-azimuth of 187° , and the bottom panels show a back-azimuth slice for a slowness value of 0.09 s/km. The event was recorded by the MKAR array at an epicentral distance of 17° and has a theoretical back azimuth of 187° (see Table 1).

To further illustrate the differences between the phase-weighted stack and phase coherence vespagrams we compare profiles (Figure 14) from the back-azimuth vespagram slices shown in Figure 13. The profiles are taken along a constant back-azimuth of 187° and represent beam power or phase coherence as a function of arrival time. In general, the two profiles exhibit a similar shape; however, the profile of phase coherence shows much sharper onset times. This is particularly true for the emergent first arrivals, as well as later less energetic arrivals. The sharpness of the phase coherence function allows more precise arrival-time measurements, since the actual arrival onset is apparent. In the case of beam power, arrival time is most easily measured from the peaks of the function; however, these zero-phase times would need to be corrected before being included in a network-based event location algorithm.

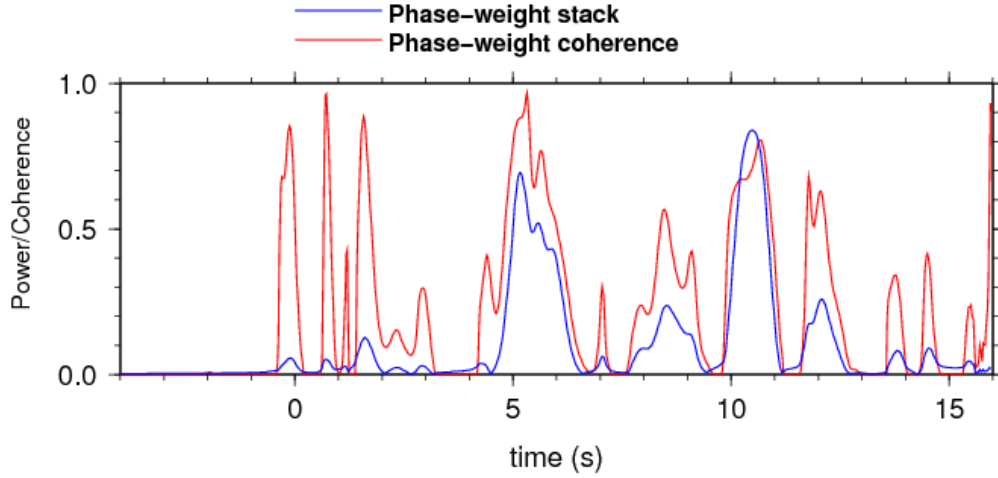


Figure 15. Profiles through the back-azimuth vespagram slices shown in Figure 13. Profiles are taken along a constant back-azimuth of 187° . The red line represents the phase-weighted coherence values, and the blue line represents normalized phase-weighted beam power. The phase-weighted coherence profile shows much sharper signal onsets.

While phase coherence stacking performs well in the analysis of far-regional arrivals observed on small-aperture arrays, there is still significant smearing in back-azimuth and slowness space. This adds uncertainty to the array measurements and subsequent phase identification. We found further improvement was possible by combining phase coherence and semblance. Semblance is defined by the following equation for vector slowness θ_i ,

$$S_i(\theta_i, t) = \frac{\left| \sum_{j=1}^M s_j \left(t + T(r_j, \theta_i) \right) \right|^2}{s_j \left(t + T(r_j, \theta_i) \right)^2}.$$

The notation is the same as in the phase coherence stack description, with time delay $T(r_j, \theta_i)$ for array element position r_j . The semblance calculation is amplitude based and can be described as

the ratio of the total beam power to the average power across all array elements. It is most sensitive to slowness values that produce high amplitude coherence. It has values that range between 0 and 1, as in the phase coherence stack. It is also beneficial to average the semblance calculation over a time gate. To combine the phase coherence stack and semblance we use a linear mixing to produce the phase coherence semblance stack (PCSS),

$$PCSS_i(\theta_i, t) = \frac{S_i(\theta_i, t) + c_i(\theta_i, t)}{2}.$$

The PCSS is a 3-D function with parameters of slowness, back azimuth and time. The combined coherence values also range between 0 and 1. An example PCSS vespagram is shown in Figure 15 for the same event shown in Figure 13, with similar slices through the 3-D vespagram. However, the filter band is slightly different (0.5 – 2.85 Hz in Figure 13 compared to 0.8 – 3.5 Hz in Figure 15), as are the color scale and axis labels.

One of the main advantages of combining the semblance with the phase coherence stack is the reduction in slowness smearing and the more clear separation of individual arrivals. This is apparent through a comparison of Figures 13 and 15. Both the phase coherence stack (Figure 13) and the PCSS (Figure 15) illuminate the highly emergent first arrivals, which are hard to discern with the eye. In the PCSS slowness vespagram, two arrivals between 0 and 1 seconds are apparent with arrival slownesses of ~11.5 s/deg and ~13.0 s/deg. In the straight phase coherence stack (Figure 13), these appear as a single arrival. Individual arrivals occurring in wave packets are also discernible in PCSS slowness vespagram, such as those that arrive between 1 – 3 seconds, which exhibit a measurable increase in slowness over time. The arrivals are also apparent in the PCSS azimuth slice, although with a lower coherence value. This is illustrative of one of the drawbacks of presenting the 3-D vespagrams as 2-D slices. For example, the azimuth slice is determined for a constant slowness value (or phase velocity; 11.1 km/s in this case), which is typically not an optimum value for each arrival. In our analyses we designed a detection algorithm to process the 3-D vespagrams to highlight arrivals that exceeded a certain coherence threshold.

We processed each event in our far-regional database using the PCSS method, and the resulting 3-D vespa grids were then run through a detection algorithm, triggering on values that exceeded 75% coherence. These detected arrivals are then stored in an associated database to be processed by τ -p methods (discussed in a later section of this report).

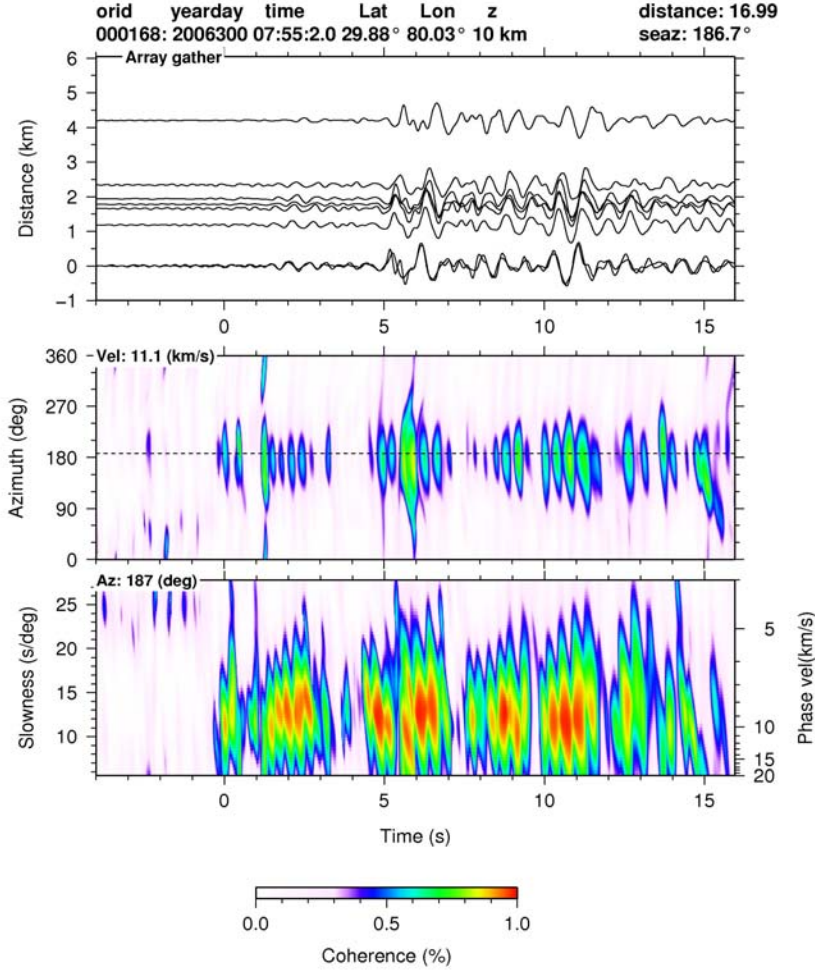


Figure 16. Example of phase coherence semblance stack analysis using data from the event in Table 1. *Top:* Slice through the 3-D vespagram at a constant phase velocity of 11.1 km/s; *Bottom:* Slice through the vespagram at a constant azimuth of 187°.

5. Wavefield Continuation Analysis to Determine Path-Specific 1-D Velocity Models

The most direct means of phase identification is through matching arrival time and slowness estimates to theoretical predictions. In complex tectonic regions such as south-central Asia, global reference models perform poorly at far-regional distances, and more specific knowledge of the along-path and near-array earth structure is required for confident primary and secondary phase identification. Therefore, we developed path-specific 1-D velocity models using two wavefield continuation analysis methods and the array measurements made using the PCSS processing in the previous section.

Wavefield continuation processing decomposes a recorded wavefield into its plane-wave components, where each phase arrival can be described by a function of intercept time (τ) and ray parameter (p) (e.g., McMechan and Ottolini, 1980). In this decomposition, τ represents an arrival's two-way travel time from its turning point at depth to a point on the surface directly above it, and p is its horizontal slowness. In a spherically symmetric earth, τ - p analysis can completely describe ray behavior.

A ray's turning depth is directly related to the earth structure and hypocentral distance along its travel path. This is illustrated in Figure 16 for rays in the *iasp91* model (Kennett and Engdahl, 1991). While the 410-km and 660-km discontinuities cause multipathing at epicentral distances less than 18° , most rays from the 8° – 18° range sample above 300 km depth; multipathing produces rays that sample multiple depths. At distances up to 28° , most rays have turned by 700 km depth, thus, to sample the upper mantle transition-zone structure requires events in at least the 8° – 28° range.

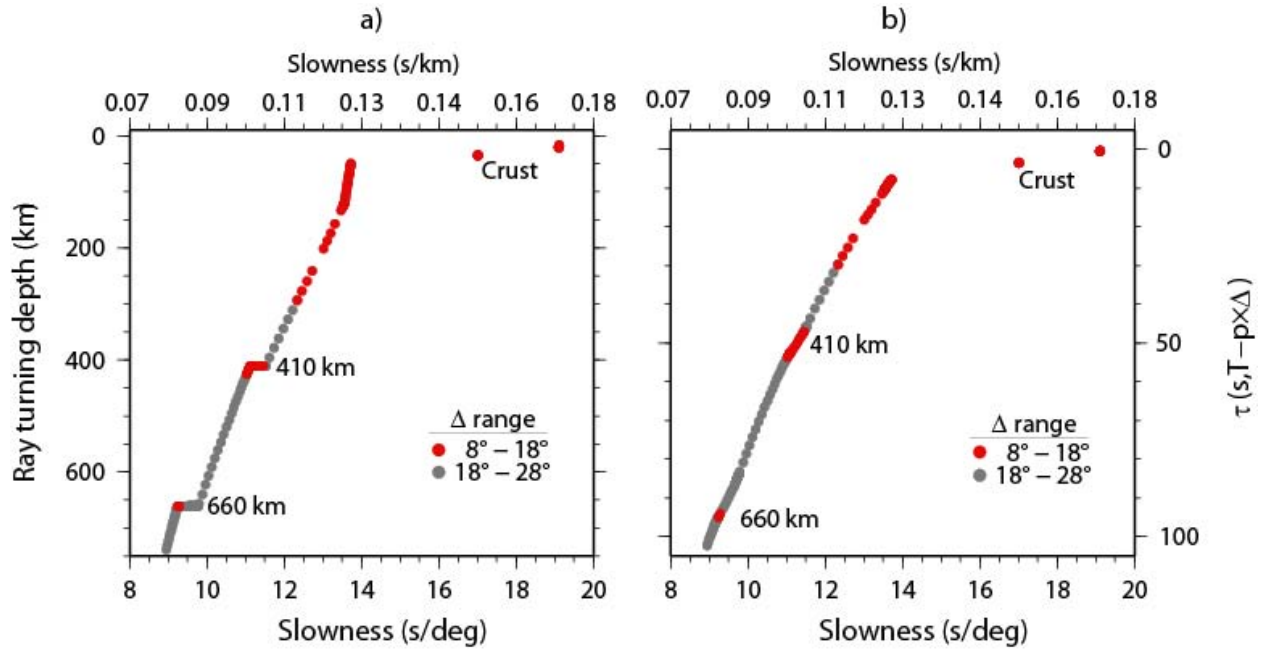


Figure 17. Illustration of the behavior of turning rays in the iasp91 1-D reference model. a) Ray bottoming depths expected for events in the 8° – 18° and 18° – 28° distance range (red and grey, respectively); b) the corresponding arrival-time/slowness (τ - p) curves.

To generalize our PCSS array measurements and explore the applicability of better 1-D earth models, we employed two separate τ - p techniques to derive velocity calibration profiles. Both techniques are based on τ - p (i.e. delay-time/slowness) methods that decompose wavefields into their components parts. The first method involves directly inverting array-based delay-time and slowness measurements to solve for a velocity-depth function (e.g., Carbonell and Smithson, 1994). The second method applies wavefield continuation techniques to array-beam record sections to accomplish the same goal (e.g., McMechan, 1984). While these methods are not new, they are not typically applied to small-aperture array data, but rather to data from long linear arrays of seismometers (e.g. Morozov *et al.*, 2005). Since we are applying these methods to records from

multiple events, we must account for the effects of differing source parameters (origin time, event depth, and focal mechanism), which may be unknown or poorly constrained. From these exercises we were able to derive models for specific regions in our study area that are based on our array observations. We discuss our application of the two inversion methods in the next two subsections.

5.1 Direct Inversion of Delay-Time and Slowness Array Measurements

The direct inversion method uses the slowness and delay-time measurements output by the PCSS array-processing as input data. The delay-time of each arrival is converted to τ using the epicentral distance and origin time information found in the ISC catalog. For most events, the PCSS vespagrams were computed for the first 18 seconds of the array seismograms. This window length captures all the $P410/P660$ arrivals and primary pP depth phases, but may miss pP phases from the 410-km/660-km discontinuities and their sP counterparts for deep events. Figure 17 shows an example of the technique we use to collect delay-time and slowness array measurements for velocity-depth inversion.

We first groomed the outliers, using a set of measurements made at MKAR consisting of 172 earthquakes that ranged from $14 - 29^\circ$ epicentral distance. This included earthquakes extending from the Hindu Kush region of Pakistan/Afghanistan to the Makran coast and Zagros Mountains of Iran. The grooming removed everything outside the $8.0 - 14.5$ (sec/deg) slowness range, thereby eliminating measurements from P-to-S scattered signals and coherent noise. We also discarded measurements that exhibited significant slowness smearing (i.e., measurement uncertainties) during the PCSS processing. Once the groomed measurements were collected, we reduce them to a single τ - p curve by computing the error-weighted-mean τ value within evenly spaced slowness bins (Figure 17b), excluding bins with only a few measurements. Averaging the τ values within a common slowness bin acts to correct for errors in focal depth by accounting for the $\pm \tau$ offset between P and pP . While this is not a perfect correction due to potentially missed phases in the array processing, the inclusion of sP arrivals, and measurement error, we have found it more effective and feasible than correcting τ on an event basis using catalog depths, which typically have large uncertainties. The averaged τ - p curves are the observations that are input into the velocity-depth inversions.

We note that there are some differences between the averaged τ - p curve from the array measurements and the *iasp91* curve. While the two curves follow the same general trend, the averaged empirical curve is not nearly as smooth as the *iasp91* curve. This may reflect measurement error in the array processing or inadequate averaging, or result from the inclusion of events from a region of variable earth structure. The averaged curve also has inflection points that are more dramatic and differ in location from those of the *iasp91* curve. In the averaged curve the main inflection points occur near 10 s/deg and 11 s/deg, compared to 9.5 s/deg (660-km discontinuity) and 11.5 s/deg (410-km discontinuity) in the *iasp91* model. This may be related to a shallowing of the mantle discontinuities and a more profound velocity contrast across them. The measured τ - p data also includes a break in the curve near 13.5 s/deg followed by a reduction in slope. These measurements come from events in the $14 - 29^\circ$ distance range. It is unclear what

causes this break (e.g., measurement error, averaging effect, or true earth structure), but it will significantly influence the shallow mantle velocity gradient.

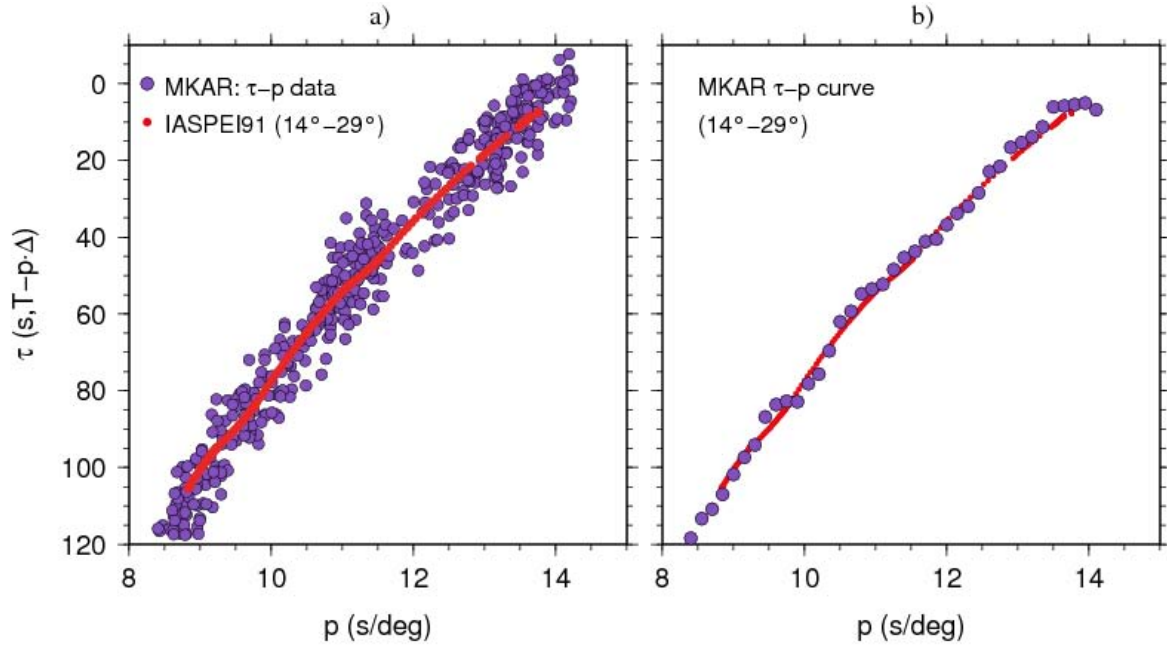


Figure 18. Sample τ - p data from the MKAR array. a) The groomed data (blue circles); red dots show the IASPEI91 (i.e., *iasp91*) τ - p curve for a surface-focus source. The range in τ for a particular slowness is caused by the difference in τ for earthquakes at different depths, rather than just measurement error. b) The averaged τ - p curve from the groomed data, evenly sampled in slowness at 0.15 sec/deg.

Figure 18 shows a preliminary velocity profile determined from the τ - p data shown in Figure 17. There are many ways to parameterize this inverse problem, and the results in Figure 18 represent only one solution. To derive the model we solved for the thicknesses of a sequence of layers that best fit the τ - p observations, using a damped least-squares formulation. For this particular inversion, we linearized the problem by assigning each slowness p to a layer representing its maximum depth of penetration (i.e. the ray turning point), which depends on the initial velocity-depth profile and is updated after each inversion iteration. The under-determined system of equations we invert is $\tau = G \cdot h$, where τ is a vector of zero-offset time observations and h is vector of model layer thicknesses. Each row of G is composed of the vertical slowness through each layer up to the turning depth for each p observation. While linearizing the inversion allows a direct estimation of model uncertainties, the final results tend to be strongly influenced by the initial model.

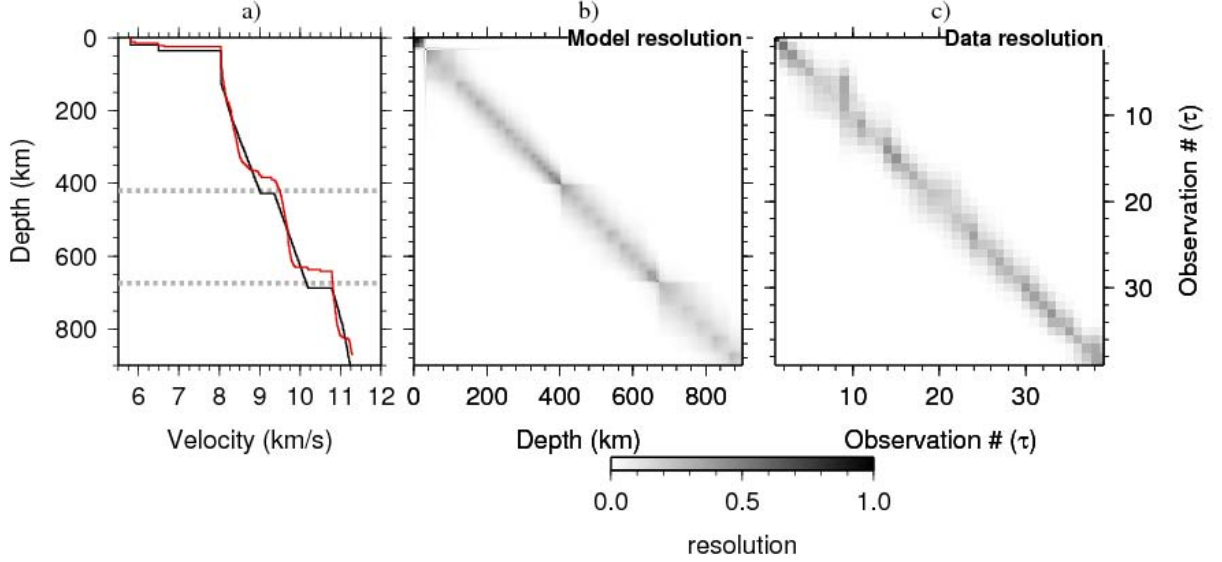


Figure 19. τ - p inversion for a velocity profile using the data shown in Figure 17. a) Final model (red) compared to the starting model (black); b) the model resolution matrix; and c) the data resolution matrix.

5.2 Wavefield Continuation Analysis Using Array Beams

The method of downward wavefield continuation (*e.g.*, Clayton and McMechan, 1981) is commonly used in exploration seismology to extract velocities from refraction profile data. To apply it to passive source seismic data, the refraction profiles are replaced by earthquake seismograms arranged according to their distances and aligned on their first arrivals.

The wavefield continuation consists of two linear transformations of the data: 1) slant stacking, which transforms the data into a p - τ space; and 2) downward continuation, which involves transformation of the p - τ data into a p - z plane. Here p is a ray parameter (horizontal component of the slowness vector), and τ is the vertical component of the travel time t . We perform slant stacking in the time domain using the following equation:

$$s(\tau, p) = \int_0^{\infty} F(\tau + px, x) dx,$$

where F is a trace observed at a distance x , and $\tau = t - px$. The p - τ wavefield can be mapped (migrated) to the depth-slowness (or depth-velocity) field using the downward continuation operator and a velocity-depth function $v(z)$. The downward continuation operator is given by:

$$\Psi(p, z) = \int_0^z (v(z)^2 - p^2)^{1/2} dz$$

At regional and teleseismic distances the velocities should be modified using the velocity flattening transformation: $\tilde{v}(z) = v(z) R_e / (R_e - z)$, where z is the depth and R_e is the earth radius.

Because a velocity model has to be chosen in order to perform the downward continuation, the inversion procedure is done iteratively. The initial velocity function(v_1^c) is chosen for the first iteration, and after the downward continuation is completed, a new velocity v_1^p is picked on the maximum amplitudes of the downward-continued data. This process is repeated using the new picked velocity until convergence is achieved. For example the convergence criterion using the root-mean-square (RMS) difference between the initial and the resulting velocities becomes $|v_i^p - v_i^c| < \varepsilon$, where ε represents some accepted tolerance value, i is an iteration number, and $|\dots|$ denotes an Euclidean norm operation.

One potential pitfall of this procedure was pointed out by Clayton and McMechan (1981). If the initial velocity is selected too high or too low at all depths, this process may not converge to a single self-consistent velocity function. Instead it may oscillate between two mutually exclusive pseudo-stable states. These two states constitute bounds on the true velocity function, because one of them is too high, and the other is too low everywhere. The bounds diverge as the depth increases, since the error accumulates with depth.

To avoid oscillatory behavior, we slightly changed the velocity update procedure. Instead of changing it to the maximum of the envelope, we found the weighted average between the velocity used for the downward continuation and the new velocity according to a formula:

$$v_{i+1}^c = a_1 v_i^p + a_2 v_i^c ,$$

where $a_1 + a_2 = 1$, $0 \leq a_1 \leq 1$, $0 \leq a_2 \leq 1$. We found that this procedure dampens the oscillations and provides convergence to an intermediate stable state.

We applied the wave continuation technique to a data “profile” composed of the earthquake observations at both the KKAR and MKAR arrays. We included shallow events spanning a geographic area from Pamir and Hindu Kush to the Afghan block and Eastern Iran. This covers epicentral distances between $3.4 - 30^\circ$ and a back-azimuth range between 200° and 250° . The hypocenter parameters for the data set were taken from the ISC catalog, which was filtered to exclude events with depths greater than 45 km. Figure 19 shows the locations of the events we used in this exercise (green and blue circles), and Figure 20 shows the record section that results when the array beams are sorted according to epicentral distance from the MKAR and KKAR arrays. We note that sparse seismicity in some segments of the selected profile creates gaps in the wavefield.

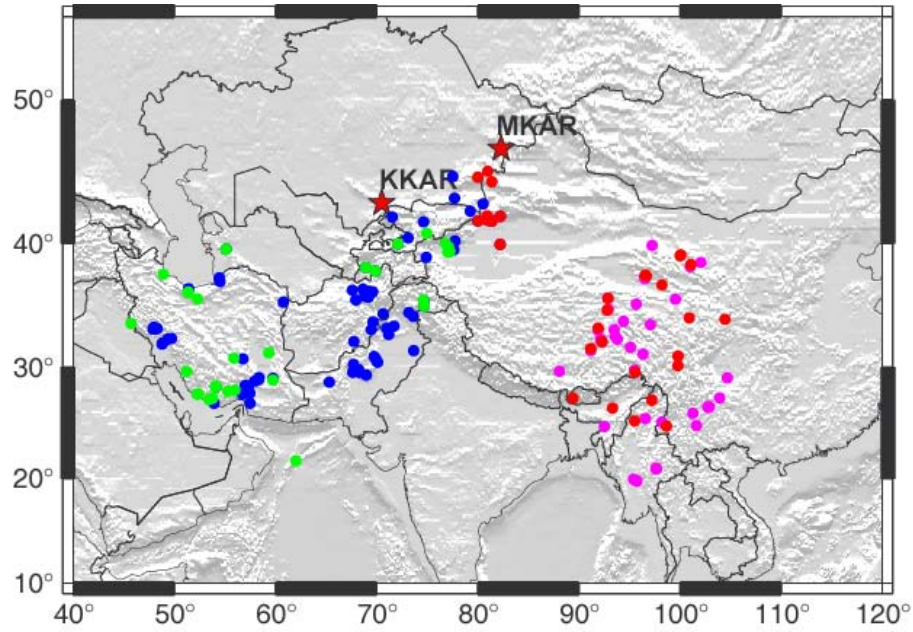


Figure 20. Map of events used to construct a record section (MKAR events – blue dots, KKAR events – green dots). The pink and red dots were not used for this exercise.

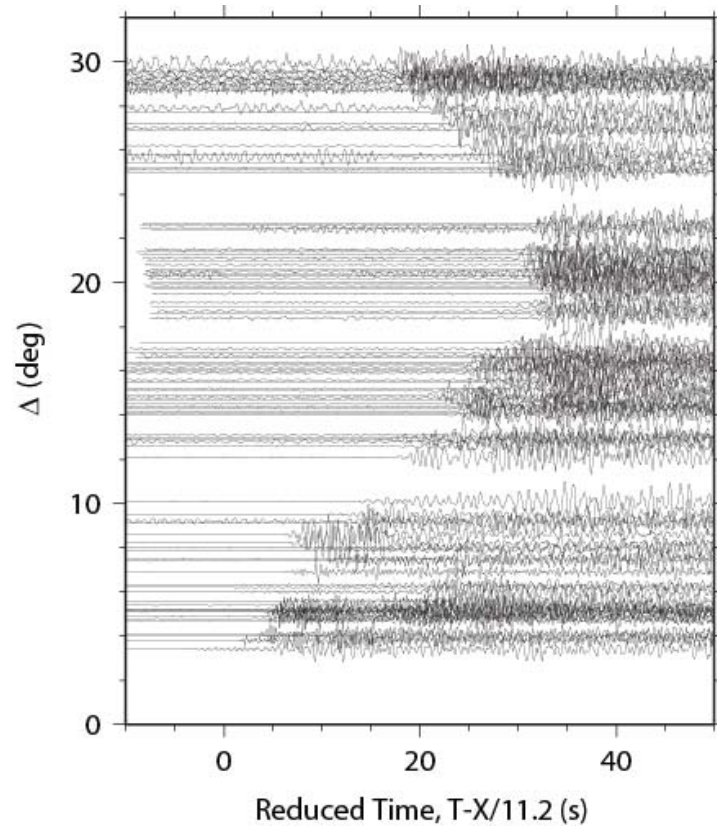


Figure 21. Record section of the data from the blue and green events shown in Figure 19. The data are plotted as a function of the epicentral distance from the MKAR and KKAR arrays.

Prior to applying the wavefield continuation technique we preprocessed the data using the following steps:

- a) Performed array beamforming using the back azimuth computed from ISC locations and the velocity predicted by *AK135* reference model (Kennett *et al.*, 1995);
- b) Band-pass filtered the array beams between 0.4 and 1.0 Hz;
- c) Applied static corrections to account for poorly known event depths; and
- d) Computed data envelopes.

After we completed the preprocessing, we performed a slant stack of the record section data, the results of which are shown in Figure 21. This slant stack represents the data space for the wavefield continuation inversion process.

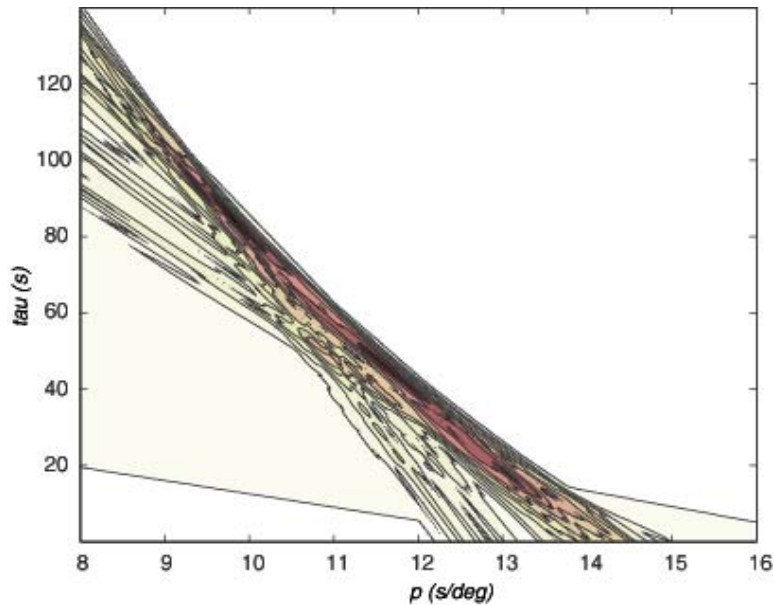


Figure 22. Slant stack of the preprocessed data from the record section.

Figure 22 contrasts the results found in the first iteration (left) versus those found after the 30th iteration (right). The AK135 model is used as the starting input in the first iteration (red line). The crustal velocity was kept constant in the inversion, using values adapted from regional studies in Kazakhstan (e.g., Kosarev *et al.*, 1993). In this case the inversion was performed using a strong damping parameter of $a_1=0.15$. The inversion process stabilizes after about 10-15 iterations, but we continue the iteration out to 30 iterations to observe the behavior of the iterative process and design an appropriate stopping criterion in the inversion. The results in Figure 22 show that the models found at the first and 30th iteration do not differ significantly from each other, mainly due to the strong damping parameter that was applied.

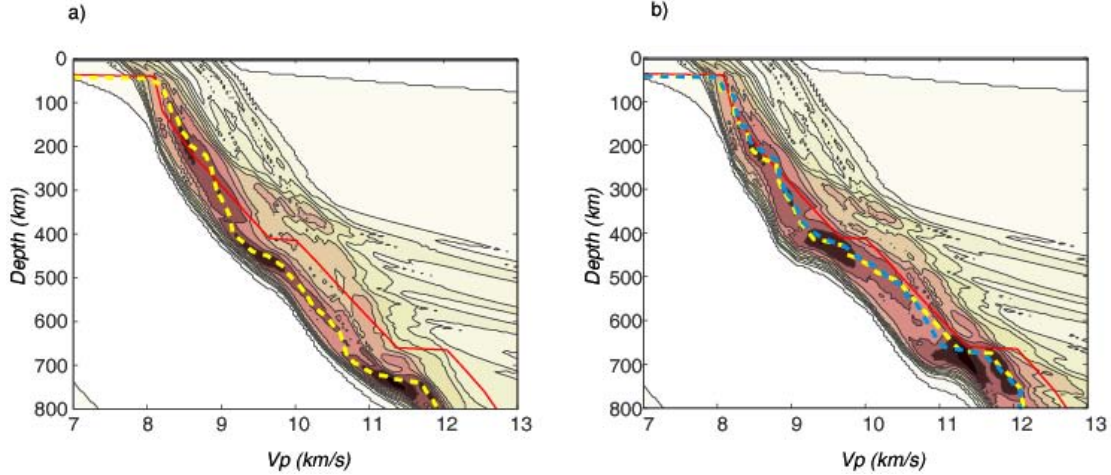


Figure 23. Velocity-depth model results following downward continuation. In both plots the AK135 model is shown as a red line and the dashed yellow line shows the final velocity model picked along the maximum of the transformed wavefield amplitude. a) Results after a single iteration; b) results after the 30th iteration. The dashed blue line shows the starting velocity-depth function used for the transformation.

We show the full set of velocity-depth functions obtained for iterations 10-30 in Figure 23a. Figure 23b shows the root-mean-square (RMS) difference between the velocity used for the continuation and the reconstructed velocity. We use the RMS difference as a measure of change in the inverse process, since we do not have a more concrete criterion to guide the fitting process. The RMS difference between the two velocities after the final iteration is on the order of 0.08 km/s, which indicates that a self-consistent model was achieved. The final velocity-depth function obtained after 30th iteration (red dashed line) shows clear 410-km and 660-km discontinuities. In addition, there is a noticeable Lehman discontinuity, expressed as an increased gradient between 220 and 240 km.

To demonstrate the effect of the damping parameter we show the results from using $a_I=1$ (no damping) in Figures 23c and 23d. In this case the process oscillates between two pseudo-stable solutions. The final RMS difference is in fact larger than the RMS at the initial iteration (~ 0.88 km/s). Figure 23c shows that the resulting pair of the mutually exclusive velocity functions (blue lines) indeed represents the bounds on the final velocity shown with the red dashed line (same as in Figure 23a). However, the starting model (AK135 model shown with the grey dotted line) is also bounded by the two states at almost every depth. We note that the resulting velocity-depth function has consistently lower velocities than AK135 through the entire transition zone.

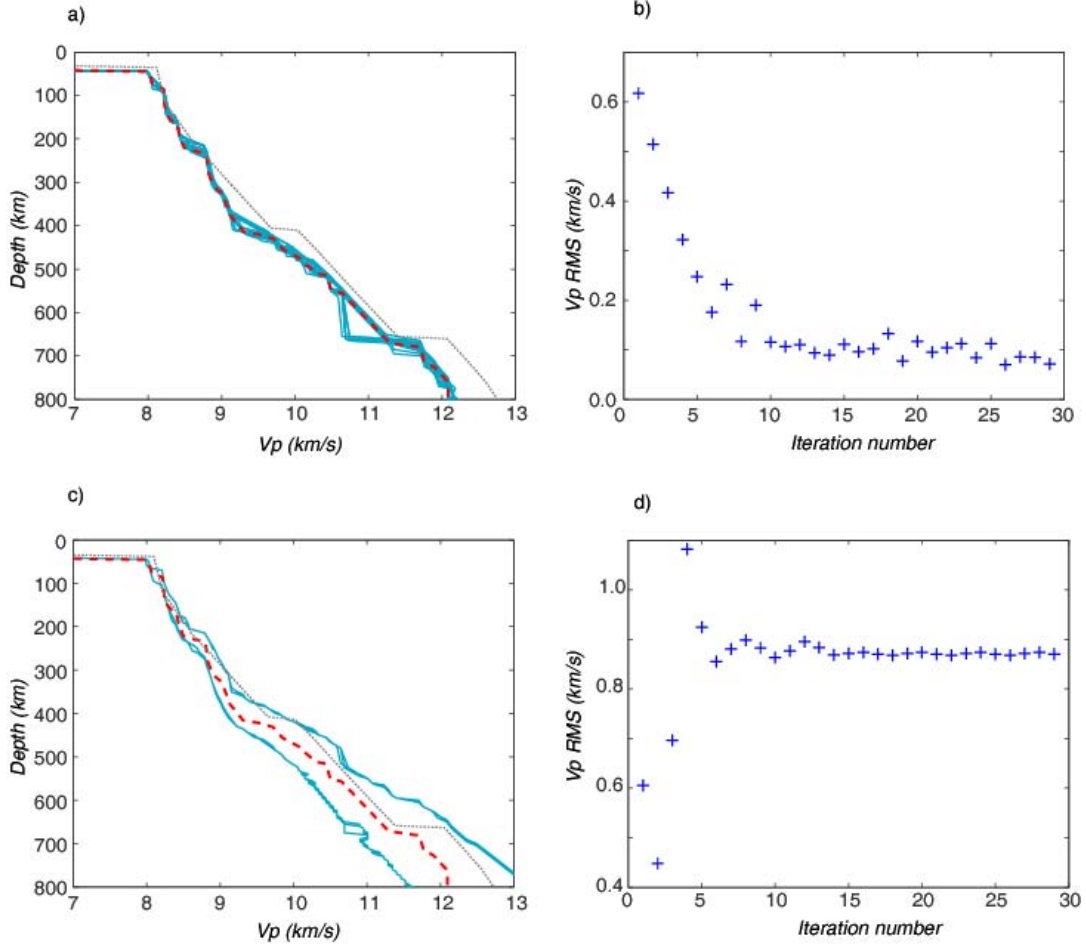


Figure 24. Results from applying wavefield continuation to earthquake data. a) Velocity-depth functions obtained as a result of the iterative process for the iterations 10-29 (blue lines). The red dashed line shows the velocity after the final (30th) iteration, and the grey dotted line shows the AK135 model for comparison. **b)** RMS difference between the velocity used for the downward continuation and the reconstructed velocity at each iteration for damping parameter $a_I=0.15$. **c)** Velocity-depth functions found by the iterative process, except with damping parameter $a_I=1$. **d)** RMS difference for damping parameter $a_I=1$.

Figure 24 shows a comparison of our preliminary velocity-depth profile derived from the wavefield continuation procedure to the IASPEI91 (i.e., *iasp91*) model. Below 400 km depth, our model exhibits moderately slower velocities than *iasp91*, and a gradient zone at the 410 km rather than a sharp discontinuity (Figure 24a). A comparison of the slowness vs. distance curves for the predicted P arrivals for each model are shown in Figure 24b. Here the differences are more apparent, and our derived model shows more structure above the 410-km discontinuity (slowness $< \sim 12$ s/deg), and a significant difference in the caustic points of both the 410-km (termination of B-C branch in Figure 24b) and 660-km discontinuity (termination of D-E branch). Some of the features we observe may be related to an inadequate distance sampling of our array beams, as well as the windowing procedure used in the initial τ - p transformation. Both of these would explain the initial appearance of the predicted 410-km and 660-km triplicated arrivals at greater distances (18°

and 20° , respectively) in our derived model than the in the *iasp91* model, where they appear at 14° and 18° , respectively.

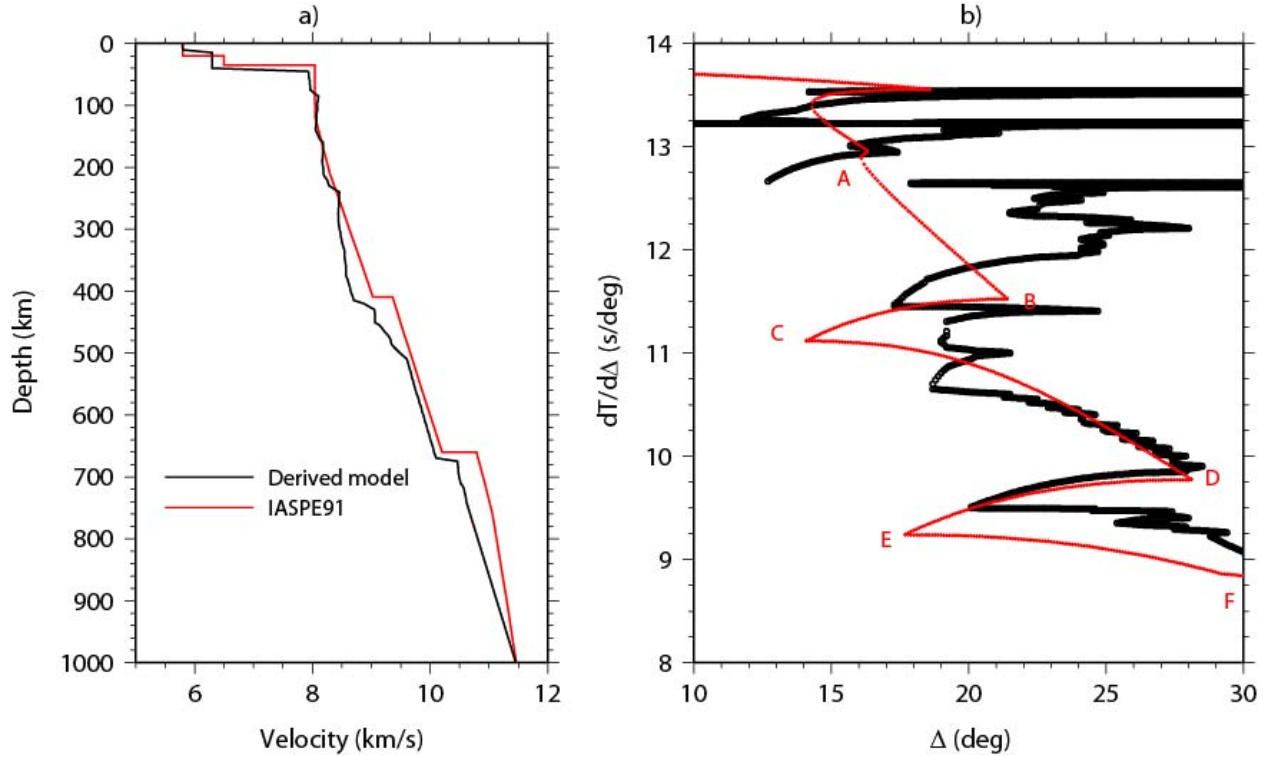


Figure 25. Comparison of the velocity-depth profile from wavefield continuation to the *iasp91* reference model: (a) derived model (black) and IASPEI91 (*iasp91*) model (red). (b) Slowness vs. distance comparison between the derived model (black) and the *iasp91* model (red) for predicted *P* arrivals.

6. Examination of Region-Specific Phase Behavior Using Waveform Clustering

To better understand the far-regional phase behavior not predicted by τ - p ray methods, we used the results from our velocity-depth inversion to synthesize suites of seismograms that are used as part of a waveform clustering algorithm. The clustering algorithm processes array beams to derive 'wavefield templates'; i.e., grouped observations with similar phase characteristics. The wavefield templates are further analyzed in a non-linear fashion by comparing them with the synthetic seismograms, looking for quantitative explanations for the phase behaviors not predicted by τ - p ray methods.

Another motivation for this effort was the strong similarity in waveform character that several groups of far-regional earthquakes in our database exhibited. This led us to hypothesize that we could group events into semi-discrete clusters for each region in our study area based on the similarity of particular waveform characteristics. By categorizing the dataset in this way, the goal was to develop a set of template events that generalize the phase behavior and phenomenon observed for each region.

As an example of the types of waveform similarities we see in our data set, Figure 25 (right panel) shows the array beams (and cumulative stack) for four seismograms from western China recorded by the MKAR array. The beams exhibit similar waveform structure in both phase arrival times and structure. This grouping of earthquakes was serendipitously found in the dataset during array processing, which led us to develop more rigorous clustering technique to find more such groupings.

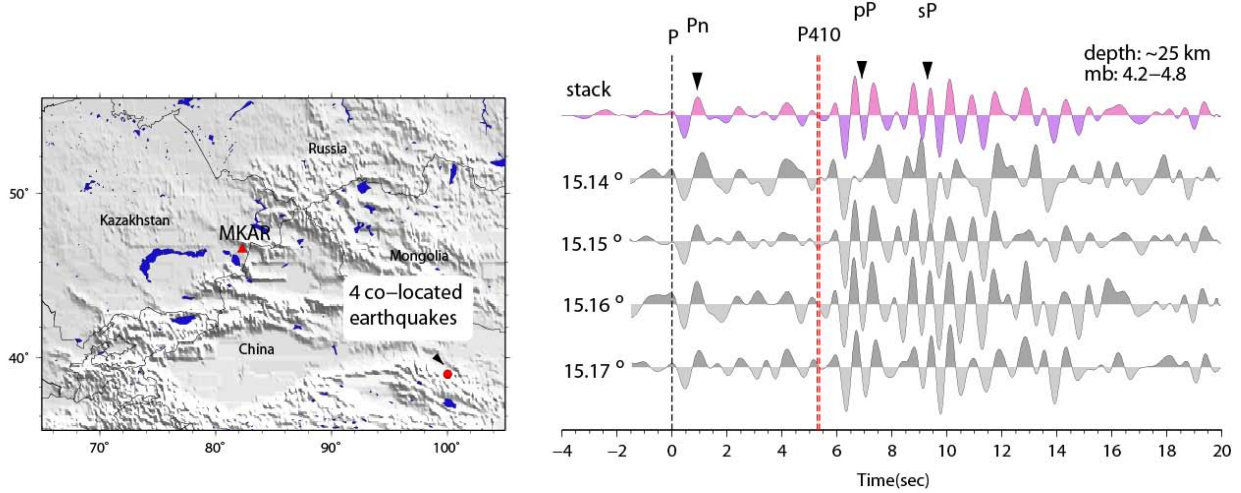


Figure 26. Left panel shows 4 earthquakes recorded at MKAR that exhibit similar phase arrival characteristics. Right panel shows the array beams (and cumulative stack), which exhibit similar waveform structure in both phase arrival times and structure.

In addition to the arrival times and slowness of the P-arrival suite, our phase-coherence semblance stacking analysis yields array beams, which are suitable low-noise records for input into waveform clustering schemes. We explored ‘partitional’ clustering methods in which we incorporate cross correlation and objective function-based classification schemes to sort our database of array beams. In partitional methods, each waveform is evaluated for membership to particular cluster groups by its degree of similarity to other cluster members in the group. The clustering method we favored is referred to as fuzzy-clustering (Bezdek, 1981). In our implementation, fuzzy-clustering finds similar seismograms based on arrival alignment by minimizing the objective function

$$J_m = \sum_{i=1}^N \sum_{j=1}^C u_{ij}^m \|x_i - c_j\|^2$$

In the above function, u_{ij}^m defines the membership criteria for each cluster group, x_i are the waveforms to be clustered, and c_j are the cluster centers (or template array-beam events) determined from the set of cluster members. The cluster centers are determined by computing,

$$c_j = \frac{\sum_{i=1}^n u_{ij}^m \cdot x_i}{\sum_{i=1}^n u_{ij}^m},$$

and the membership values are determined from

$$u_{ij}^m = \frac{1}{\sum_{k=1}^C \left(\frac{\|x_i - c_j\|}{\|x_i - c_k\|} \right)^{2/(m-1)}}, m > 1,$$

where m is the fuzziness value. Larger values of m relax the criteria for membership to a particular cluster group. The cluster centers change as new members are added and subtracted to the group, and limited control over the clustering results can be made by predefining the cluster centers. For each waveform and each cluster, the membership function u_{ij}^m has a value between 0 and 1, where values closer to 1 reflect a stronger similarity of the waveform to the cluster center.

The clustering is carried out as an iterative optimization of the objective function J_m , in which the cluster centers (c_j) and membership matrix (u_{ij}^m) are updated at each iteration step. Iterations are stopped for $\max_{ij} \{ |u_{ij}^{k+1} - u_{ij}^k| \} < \varepsilon$, where ε is the analyst-defined convergence limit (between 0 and 1) and k is the iteration step.

Our general algorithm for determining waveform clusters using the above scheme is composed of the following steps:

- 1) Choose a set of waveforms to be clustered and the number of clusters to search for.
- 2) Cross correlate the waveforms so that they are time aligned.
- 3) Initialize the membership matrix ($u_{ij}^m, k = 0$).
- 4) Calculate the cluster centers (c_j^k) for the current membership matrix.
- 5) Update the membership matrix ($u_{ij}^{m,k}, k = k + 1$) with the current cluster centers.
- 6) Calculate the convergence error.
- 7) Stop the iterations if the convergence limit is reached, otherwise return to step 4.

Figure 26 shows an example cluster group determined using a set of 167 array beams from varying geographic regions. These array beams were clustered into 25 separate groups, and each group was then further separated into 2-5 groups. In this particular example, 15 seconds of each waveform were processed, beginning 0.5 seconds prior to the initial arrival and including 14.5 seconds of P coda. Before clustering, the waveforms were time-aligned to the maximum correlation lag in this 15 second window. For many of the seismograms, this resulted in the waveforms being aligned along the $P410$ arrivals, since these arrivals typically have the largest amplitude in the window. In latter analyses, we limited the cross-correlation to the first arrival window to better understand the effects of the 410 discontinuity on arrival-times and depth phases.

As evidenced by the members of the sub-group in Figure 26, the clustering algorithm grouped waveforms that generally have similar $P410$ phase structure, regardless of the $P410$ arrival time (arrival time relative to the first arrival), and that tend to have emergent first arrivals. When sorted by increasing correlation lag time, the group members show a positive move-out time of the $P410$ phase. For a common earthquake depth, a positive move-out of the $P410$ arrival is expected for

decreasing earthquake distance, but for this group, earthquake distance does not correlate with the move-out time (Figure 26: right column). There are several factors that could explain this oddity. Since the waveforms grouped in Figure 26 are from different regions, variations in the depth of the 410-km discontinuity would affect the arrival time of the *P*410 phase. Increasing earthquake depth would also affect the *P*410 arrival time. A more mundane explanation may be that in some instance the large amplitude phase in Figure 26 is not the *P*410 phase.

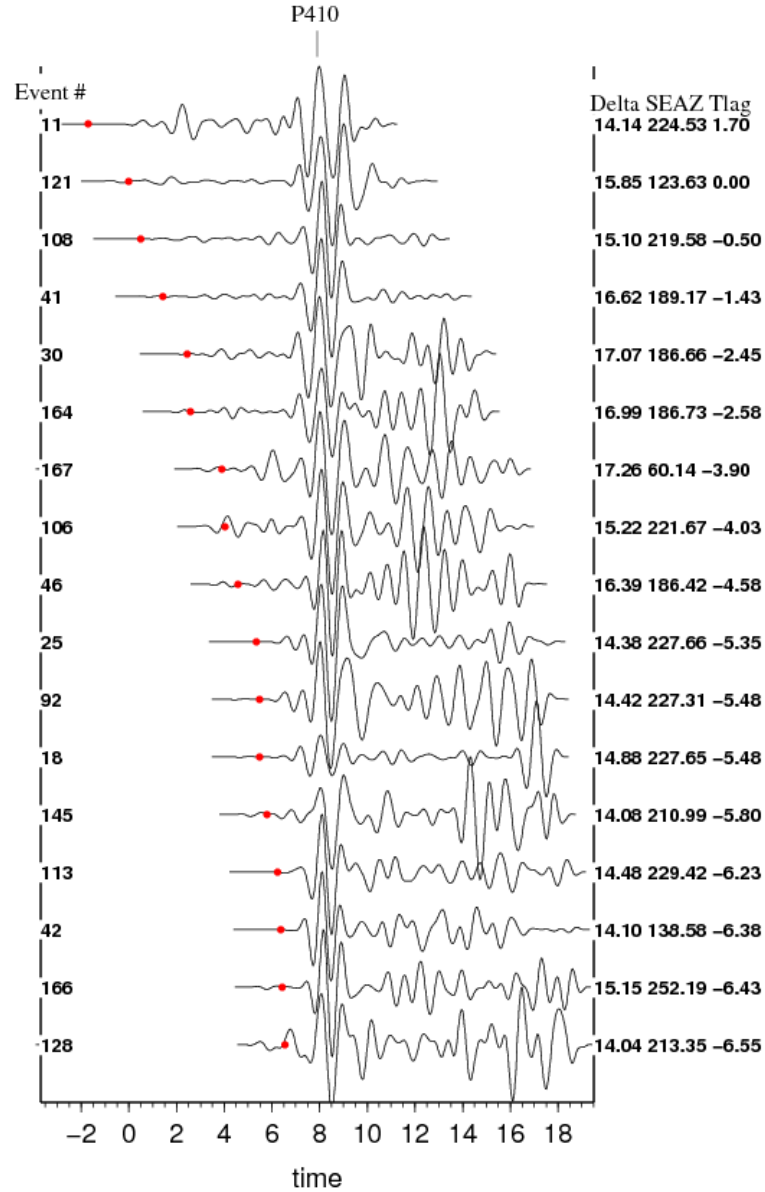


Figure 27. An example cluster group found from processing 167 array beams. The waveforms exhibit similar *P*410 phase structure and are time-shifted based on the maximum correlation lag time. Red dots mark the first arrival, and numbers on the left column are the event ids. On the right is shown the earthquake distance (Delta; degrees), the station-to-event azimuth (SEAZ; degrees), and the cross correlation lag time (Tlag; seconds).

While the cluster group shown in Figure 26 is interesting, we wanted to find cluster groups that exhibit both a similar arrival-time and phase structure. We noted that the cross-correlation of long time windows tended to align the waveforms along *P*410 phase. This biased the clustering results towards groups with similar *P*410 phase structure, to the detriment of other phases in the records. In order to minimize this, we first modified our algorithm to time align on the first arrival, rather than the largest amplitude arrival. Second, we explored different minimization measures. The cluster group in Figure 26 was found using an L2 norm, but this measure can be sensitive to noise in the data and variances in arrival amplitude (and total power) between cluster members. The variance in arrival amplitude can be a result of different focal mechanisms for the different cluster members. We found improved results by optimizing the objective function with L1 norm, which is less sensitive to data noise, and a semblance measure, which is less sensitive to amplitude variance and polarity swings. Our final implementation tracked four measures to compare the trade-offs of each: L1 norm, L2 norm, semblance, and the maximum cross-correlation coefficient.

Other modifications we have made to our algorithm include processing the Hilbert envelopes of the waveforms (calculated after cross-correlation), and processing waveforms from specific regions rather than the whole dataset at once. Using the Hilbert envelopes removes the amplitude polarity information from the waveforms, which allows earthquakes with difference source mechanisms but similar arrival time structure to be grouped. This is an important factor when attempting to group events from specific geographic regions where the source mechanisms were highly varied for small magnitude events.

For example, Figure 27 shows the cluster group and associated wavefield template that results from applying our modified waveform clustering algorithm to a set of events recorded at the MKAR array in the 14 – 18° distance range. In this example the algorithm clusters 78 events from northern Pakistan into 5 groups, with 12 – 22 members per group. To account for some source effects, the cluster membership is applied to the Hilbert envelope of the beams, although we plotted the raw beams in Figure 27. We chose the cluster groups based on an L1-norm distance measure and aligned the array beams prior to clustering using multi-channel cross correlation (VanDecar and Crosson, 1990) applied to the first four seconds of each beam signal. As previously mentioned, we found the alignment of the beams to be beneficial to the clustering procedure. However, the length of the cross-correlation window is an important variable. For example, if the window is too long, the array beams align on the maximum amplitude signal in the record. For some beams the maximum amplitude arrival may occur early in the seismogram, while for others it occurs much later. This can result in some unusual clustering of events that seems counter-intuitive. For this reason, we find clustering methods based strictly on cross correlation, as used in other types of studies (e.g., Menke 1999; Ferretti *et al.*, 2005; Barani *et al.*, 2007) were not suitable for a dataset such as ours.

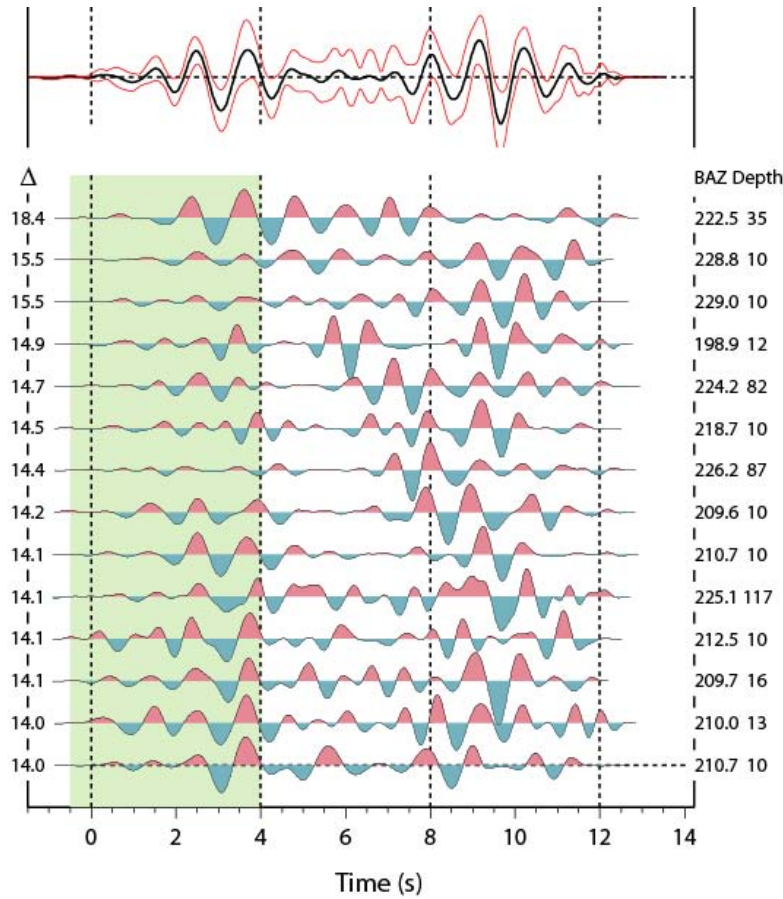


Figure 28. Wavefield clustering to generate a wavefield template. The bottom panel shows the cluster members sorted by epicentral distance (shown on the left). The green band highlights the region of cross correlation. The top panel shows the computed wavefield template (black) and 1- σ deviation (red).

In the example shown in Figure 27, the resulting cluster members include earthquakes that are near the 14.3° distance range, but some more distant earthquakes are also included. The earthquake depth range is also variable, but may be due to poorly constrained catalog depths. In general, the cluster members show consistent waveform structure in the cross-correlated portion of the signal. Later arrivals show more variability between the cluster members, but still appear to align well at approximately 8 seconds and later. The most variability occurs between 4 and 8 seconds delay time, where some records show large amplitude arrivals while other show little signal. Some of this variability is likely due to differences in earthquake distance, triplicated arrivals, and the presence of depth phases.

A further example, shown in Figure 28, depicts some of the template beams that result from other cluster analysis runs. This particular example shows the results from clustering 80 earthquakes within a back-azimuth range of $190 - 230^\circ$ from the MKAR array, which includes events from northern India and northeast Pakistan. The clustering produces 4 template beams, which qualitatively appear to exhibit similar polarity and arrival structure for the first 4 seconds signal. This likely implies a similar source mechanism for most of the 80 earthquakes.

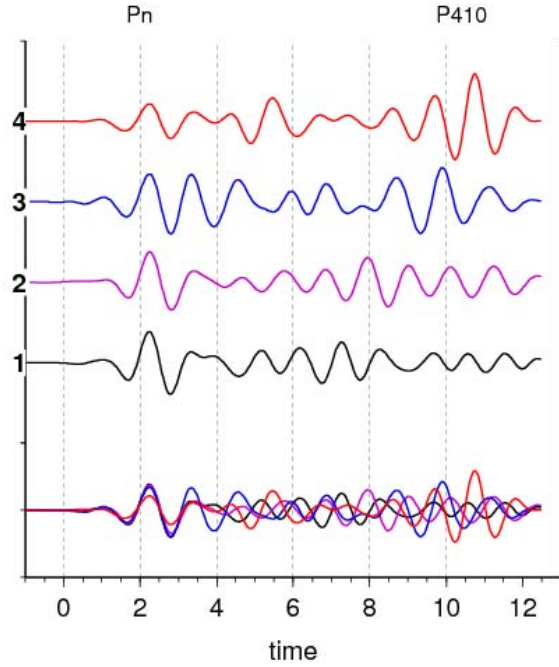


Figure 29. Template beams from the cluster analysis of 80 MKAR recorded events in the $190 - 230^\circ$ back-azimuth range. The top 4 traces are the individual template beams, which are shown overlain at the bottom of the panel. The traces are aligned on the P_n phase and filtered in the 0.03 – 1.0 Hz band. The P_{410} phase is also labeled. At Trace 4 (red) P_{410} arrives ~10 seconds after P_n , while at Trace 1 (black) P_{410} arrives ~6 seconds after P_n .

After the first 4 seconds, the template beams are more dissimilar, which is likely related to differences in earthquake depth and distance between the events that compose each template beam. The main feature in this part of the record is the large-amplitude P_{410} wave packet that arrives between 6 and 11 seconds after P_n . The arrival-time moveout of this wave packet is related to earthquake distance, and this feature should be verifiable by modeling. In general, the clustering analysis appears to produce reasonable clustering groups. However, our main objective was the resulting template beams, which we view as generalized waveforms that are representative of particular source regions.

A primary goal is to be able to explain the waveform structure of the template beams as a function of earthquake depth, earthquake distance, and the depth of the 410-km discontinuity. To fit the template beams we devised a grid-search scheme that finds the minimum L_2 -norm between the individual template beams and a suite of synthesized waveforms. We used a reflectivity method to produce the synthetic waveforms (Kennett, 1988). The synthetics were generated for a distance range of $14 - 18.8^\circ$ at an interval of 0.1° and an earthquake depth range of 2 to 60 km at an interval of 2 km. For a single source mechanism, this modeling exercise produces 1470 synthetic waveforms. Figure 29 shows an example earth-flattened velocity model with a 70-km thick crust, which tapers into the AK135 reference model in the upper mantle. The model also includes a gradient zone on the 410/660 km discontinuities, thereby incorporating the results of the τ - p

transformations developed in the previous section. Some example synthetic waveforms from this model are shown in Figure 30.

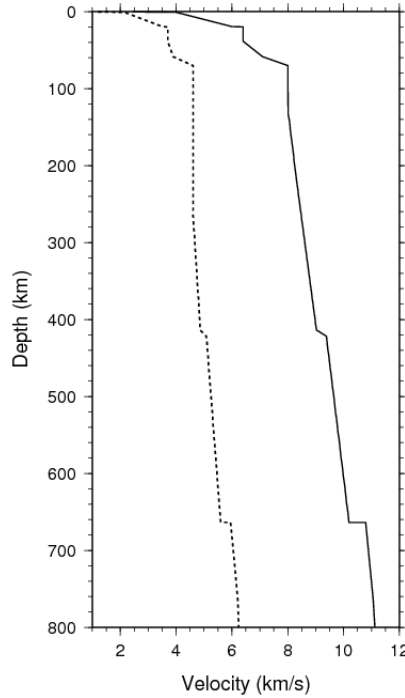


Figure 30. Velocity model used to generate synthetic waveforms. This is an earth-flattened model that tapers into AK135 in the upper mantle. P velocity is denoted with a solid line, and S velocity with a dashed line.

The grid-search minimization algorithm filters the synthetic waveforms to the same frequency band as the template beam. The synthetics are then cross-correlated to the template beam to time-align the waveforms, using a 1 - 4 second window after the first arrival. An $L2$ -norm is computed for each synthetic using a 12 - 18 second time window and the best-fitting solutions are found.

Results from the grid-search minimization algorithm are shown in Figures 31 and 32, for two template beams shown in Figure 28 (beam templates 2 and 3). In our current implementation the only free parameters are earthquake depth and distance, and our velocity model is the one shown in Figure 29. The source mechanism is a north-south striking thrust fault with a 45° dip. While this is a common mechanism observed for northeast Pakistan, this particular region also exhibits strike-slip faulting, normal faulting and oblique-slip faulting.

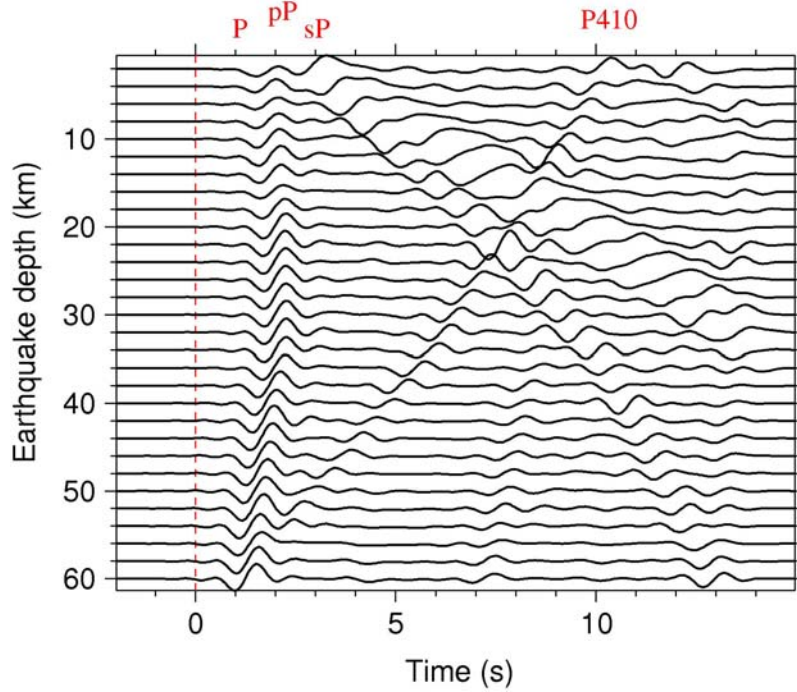


Figure 31. Example synthetic seismograms for the waveform template-fitting grid search. This example shows a seismogram gather for a range of event depths but constant epicentral distance. Note the moveout of the *P410* phases as a function of earthquake depth, and the interference between depth phases and *P410* for events depths between 10 and 20 km.

Figure 31 shows the grid-search results for template beam number 2 (see Figure 28). In general, the best-fitting synthetic waveform captures the basic structure of the template beam (top panel of Figure 31). The first arrival and the *P410* arrival packets fit well, although the synthetic does not precisely match all the features of the first arrival. Smaller amplitude arrivals are more poorly fit, but do exhibit similar structure as the template beam. In the bottom panel of Figure 31, multiple minima are observed, indicating that multiple synthetics fit the data equally well. There is a range of distance solutions for an earthquake depth of 22 km and another for an earthquake depth of 28 km. Multiple minima are not surprising given the nature of the grid search.

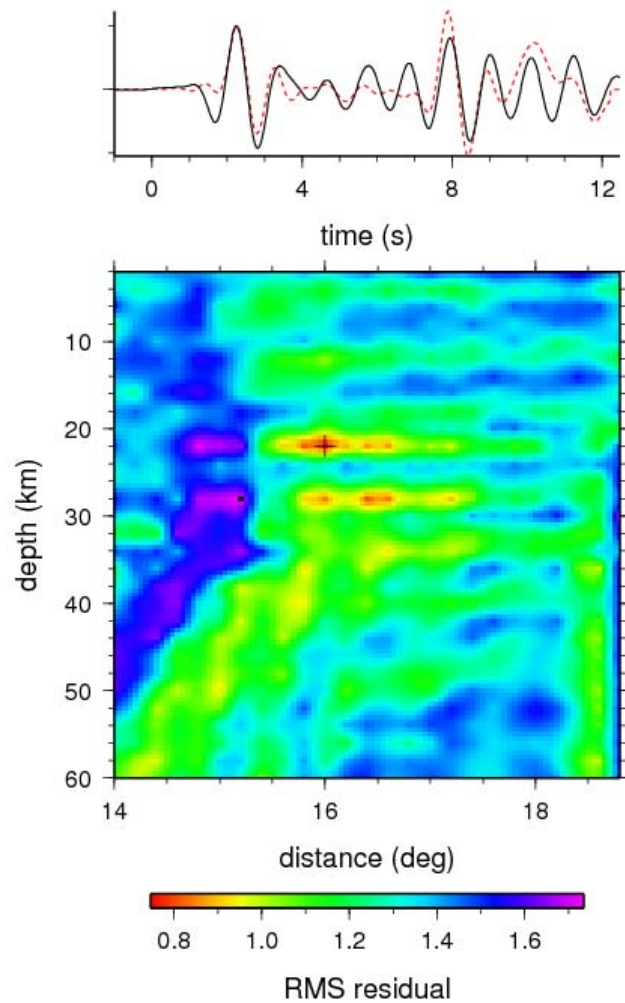


Figure 32. Example of the waveform fitting for template beam number 2 shown in Figure 28. The top panel shows the template beam (black) and the best-fit synthetic (red dashed). The bottom panel shows the root-mean-square residual for each synthetic waveform as a function of variable earthquake depth and distance. The warm colors represent waveforms that fit the data better.

Figure 32 shows the grid search results for template beam number 3 (Figure 28). In this case, the best-fitting synthetic also captures the general structure of the template beam. However, the overall fit is worse than the example of Figure 31. While the timing of first arrival and *P*410 arrival is well matched, their amplitude is not. Some of the amplitude mismatch may be caused by an inappropriate choice for the source mechanisms. The consequence of the poorer waveform fit is multiple solutions, which, for this example, include earthquake depths that range from 26 to 60 km and a distance range of 14.2 to 18°.

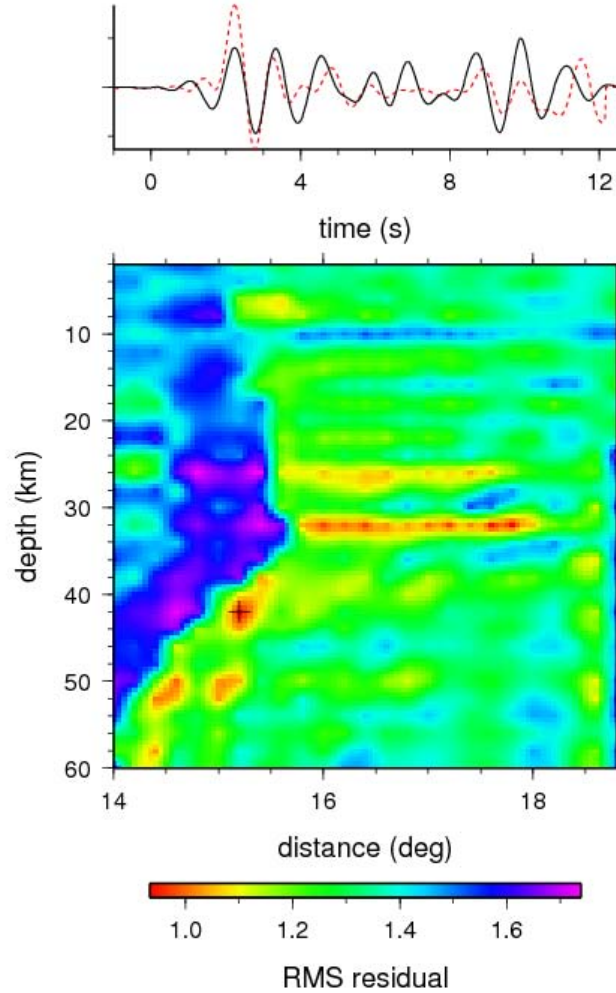


Figure 33. Example of waveform fitting for template beam number 3 shown in Figure 28. The top panel shows the template beam (black) and the best-fit synthetic (red dashed). Bottom panel shows the root-mean-square residual for each synthetic waveform where earthquake depth and distance vary. The warm colors represent waveforms that fit the data better.

In general the quality of the waveform fits were quite surprising given the crudeness of the grid search algorithm. This suggested that the waveform templating scheme was able to capture the generalized far-regional arrival structure for particular regions. One element of the grid search that remains to be addressed is the best way to select a source mechanism for the synthetics. The waveform templates are essentially weighted stacks of groups of seismograms that likely have differing source mechanisms, and it is unclear how these differing mechanisms are reflected in the templates. A more complicated approach would be to try a source inversion prior to performing the grid search.

7. Studies of Near-Array Earth Structure

In a supplemental task undertaken during this project, we studied the effects of near-receiver structure on the wavefield to separate it from path-related effects that arise from interaction with the mantle transition zone. To accomplish this we applied teleseismic array calibration techniques, including receiver functions, polarization analyses and analysis of *PcP* arrivals, using earthquake data observed 30 – 90° from the MKAR and KKAR arrays. The purpose of using teleseismic signals for these analyses was to limit the effects from the interaction with the mantle transition zone and produce array calibration information that is independent of the far-regional observations.

We collected 3-component broadband data from over 300 teleseismic events for each of the arrays and performed polarization analysis to determine a back-azimuth residual. The residuals represent the deviations from the great circle path of the published epicenter. The back-azimuth residuals are plotted as a function of event position in Figure 33 for both MKAR and KKAR. The residuals have a range of $\pm 20^\circ$, and a fair amount of scatter. As Figure 33 demonstrates, there is a paucity of information in at least one of the quadrants surrounding the arrays, but there are enough data to postulate a dipping Moho at KKAR that causes a predominantly negative residual to the southeast. This would be sensible in terms of the geology near the array, which is near the edge of deepening crust. The results at MKAR are less clear-cut, as the residuals vary significantly as a function of azimuth. This may indicate a variety of conditions beneath the array, including a flat Moho with significant local crustal heterogeneity. We have found that the far-regional data also indicate significant back-azimuth residuals at MKAR. One of the objectives of this analysis was to determine a correction factor for the near-array structure (Moho dip) that could be used to improve the far-regional array processing measurements of slowness and back azimuth. However, common methods (e.g., Niazi, 1966) applied to determine the dip of the Moho below the arrays with these data resulted in highly non-unique solutions, due to paucity of data and outliers. Assuming a single dipping interface, for KKAR we get a strike solution of N45°E and a dip of $9 \pm 6^\circ$. For MKAR we were unable to determine a solution, which led us to examine other methods to determine the near-array structure, which we describe in the following subsections.

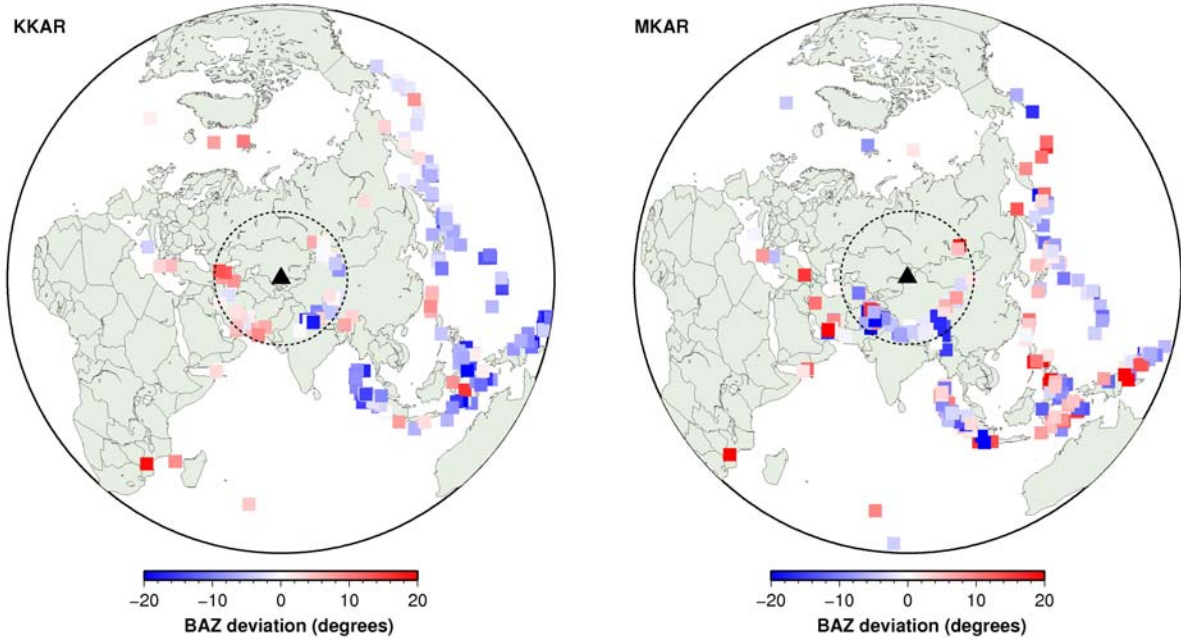


Figure 34: Back-azimuth residuals found from polarization analysis using a large data set of teleseismic events observed at MKAR (right) and KKAR (left). The dashed line marks the far-regional distance limit. The residual pattern at KKAR is more coherent, which likely indicates dipping Moho structure beneath the array.

7.1 Near-Array Earth Structure from Receiver Functions

Earth structure below an array can have a profound effect on the observed back-azimuth and slowness measurements. Near-array structure is typically accounted for by correcting the array-based measurements to theoretical values. For example, published earthquake epicenters are used to determine a theoretical back-azimuth angle to the array, and a 1-D Earth model can be used to compute expected ray parameters. In the case of a single dipping interface (e.g., the Moho), the azimuth and slowness residuals relative to the theoretical values have a sinusoidal pattern with respect to back azimuth. The amplitude and phase of these patterns can be used to solve for dip and strike of the interface, and a correction can be computed for each event based on its observed back-azimuth angle. This method works well when the orientation of the interface can be uniquely determined, if two conditions are met: 1) the near-array structure must be the phenomenon causing the anomalous residuals (i.e., there are no other path-specific effects); 2) the residuals must exhibit systematic behavior with respect to back azimuth.

We observe both back-azimuth and slowness anomalies at the KKAR and MKAR arrays, where azimuth residuals are 20° in some instances (Figure 33). However, most far-regional events occur to the south of the arrays with no events to the north. This makes typical array calibration difficult and highly uncertain. It is also not clear how many of the observed anomalies are due to near-array structure. To try to obtain a more accurate accounting of the near-array structure, and thus improve our array measurements with a correction, we employed receiver-function techniques to image the structure below the arrays. Our goal was to separate near-array effects on

the azimuth and slowness measurements from the along-path effects by accounting for the near-array structure independent of the array measurements. Determining near-array structure from receiver functions has potentially several benefits over array-based methods: 1) only the near-array structure is imaged, and far off path effects have no influence, 2) earth structure is not determined from the measurements to be corrected (the array measurements in our case), and 3) teleseismic events used in constructing the receiver functions are more azimuthally distributed compared to the far-regional events.

Figure 34 shows the effects that dipping structure has on receiver function record sections. In this synthetic case, the earth model is a simple dipping Moho (strike = 0° and dip = 10°) over a half space. The receiver functions are computed for an azimuth range of $0 - 360^\circ$ and a constant ray parameter.

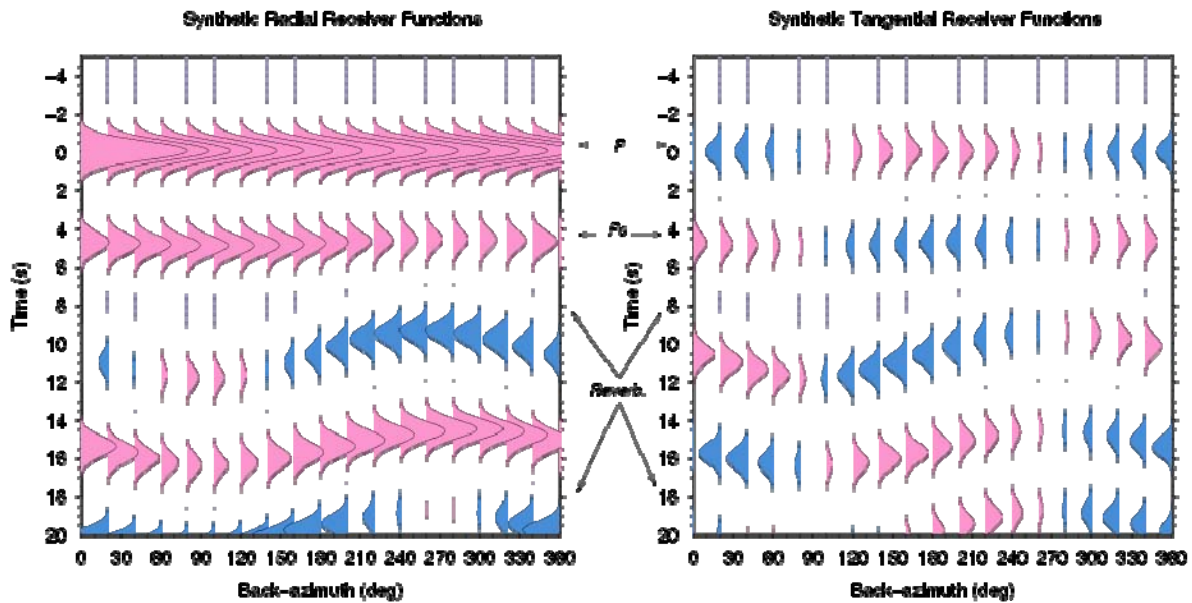


Figure 35. Synthetic receiver functions images for a 10° dipping Moho over a half-space. *Left:* tangential receiver functions; *Right:* Radial receiver functions. Positive amplitudes are red and negative amplitudes are blue. The receiver functions are aligned on the zero-phase onset time, and the main phases are labeled.

As seen in Figure 34, the dipping Moho structure causes both amplitude and arrival-time effects. The main P_s phase from the Moho shows an amplitude decay in the radial components (SV energy) and a varying amplitude polarity (sinusoidal) in the tangential components (SH energy). The reverberations mimic the polarity reversals, but also exhibit a time delay that depends on whether the signal is traveling up-dip or down-dip. The phase and amplitude of the sinusoidal polarity changes are a function of the strike and dip of the interface and thus deterministic.

For the MKAR and KKAR arrays, we computed receiver functions using a time-domain deconvolution with data from the single 3-component instrument installed at each array. Figure 35 shows distribution of teleseismic events, displayed as the Moho P_s conversion points, around each

array. Several hundred receiver functions are computed for each array. The distribution for the MKAR array is more azimuthally complete than the KKAR array.

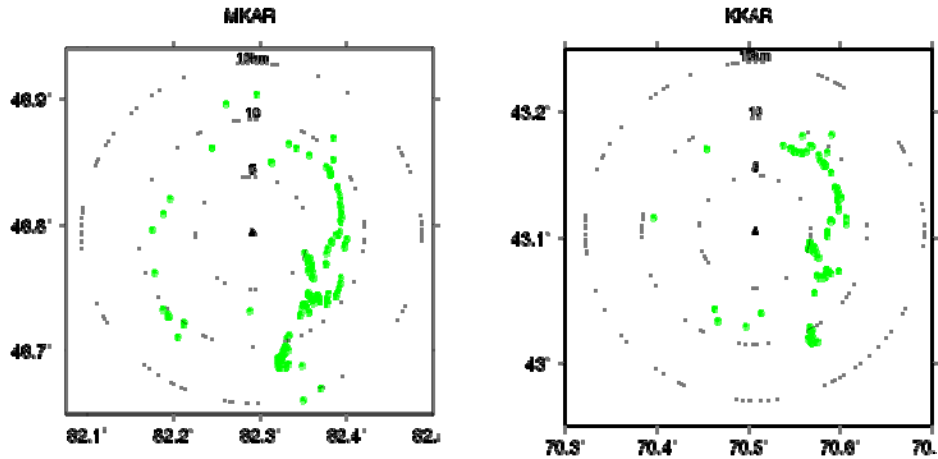


Figure 36. Azimuthal distribution of teleseismic events used in the receiver function calculations. The green dots mark the Moho conversion point for each of the receiver functions.

We compute radial and tangential receiver functions using a time-domain deconvolution method, and then form azimuthal record sections from the receiver functions. The record sections (Figure 36 and 37) are constructed by stacking receiver functions at constant azimuth spacing. To account for variation in ray parameter of the teleseismic events and to minimize scattered energy, we use a 2-D Gaussian weighting function, where the weight is a function of proximity to the back-azimuth stacking point and ray parameter. In this manner, we are able to construct evenly sampled (in back azimuth), smoothed record sections that can be used in subsequent analysis.

The main P_s converted signal at both MKAR and KKAR has a delay of ~ 3.5 seconds for the high-frequency band. It is most obvious in the radial component sections. At different back azimuths it shows some variation in arrival time and amplitude, indicating a non-planar conversion interface. Preceding this phase is a large amplitude negative pulse, which may be related to a low-velocity zone near the surface. Later arriving reverberations are also apparent in both the MKAR and KKAR sections and show variations with back-azimuth. Coherent energy is apparent on the tangential component sections, which is typically indicative of dipping structure or, in some cases, anisotropy. Coherent energy on the tangential components is clearest in KKAR record sections, where amplitude polarity changes are also seen. However, observed phases and the coherency of the record sections seem to have frequency dependence. At lower frequencies, the main P_s phase is less prominent and the tangential record sections are less coherent (not shown). This may be related to the nature of the velocity contrasts across the discontinuities below the arrays, and will likely not be sorted out from our straightforward analysis.

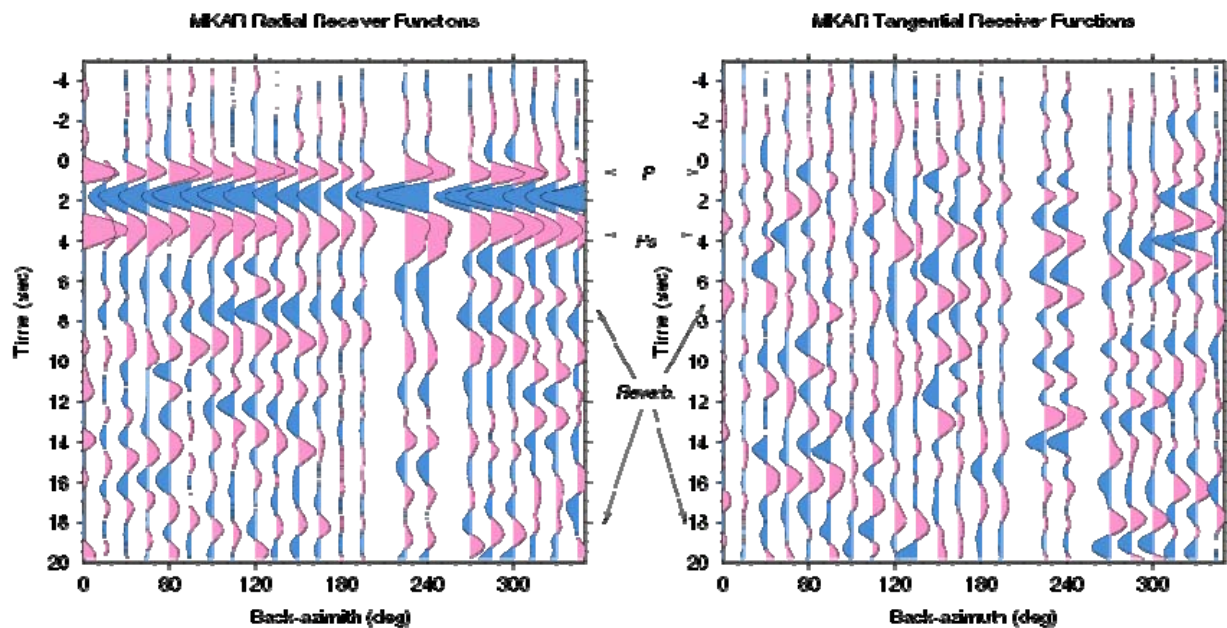


Figure 37. MKAR receiver-function record sections. The receiver functions are aligned on the minimum-phase time and have been filtered between 0.1 to 0.4 Hz.

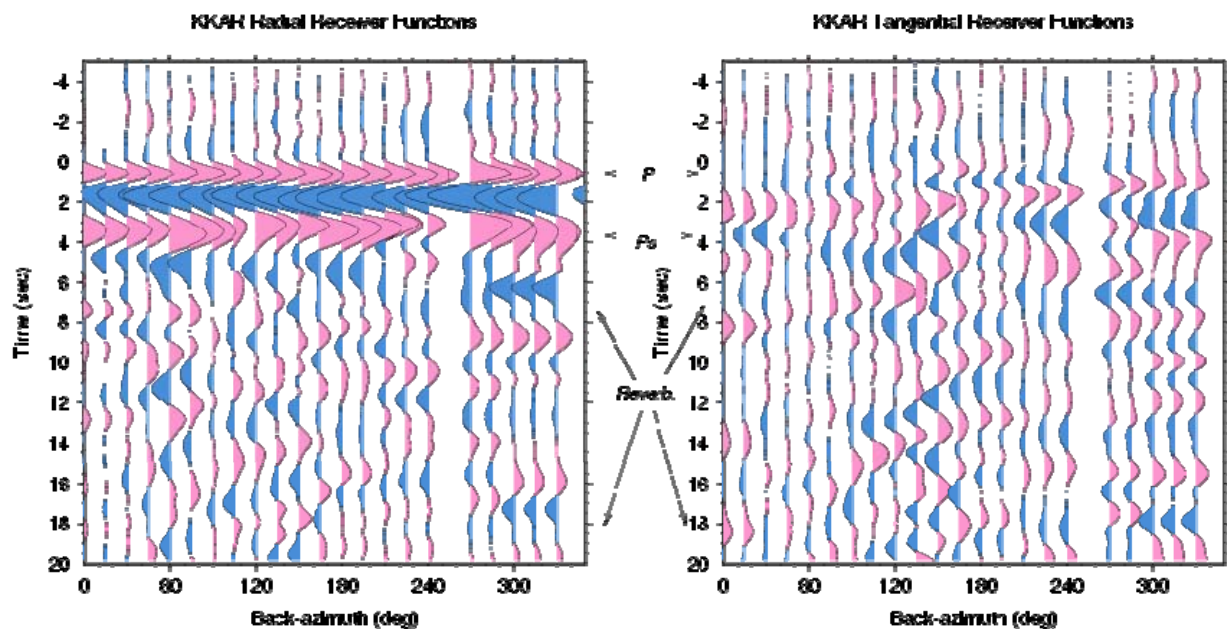


Figure 38. KKAH receiver-function record sections. The receiver functions are aligned on the minimum-phase time and have been filtered between 0.1 to 0.4 Hz.

The moveout of the radial component reverberations and the existence of coherent energy on the tangential components receiver functions seem to imply that the earth structure below the arrays is not laterally homogeneous, as we expected from the array measurements. In order to understand the earth structure we utilize a simple forward modeling approach. We start with a simple flat-layer velocity model determined from inverting a cumulative stack of the radial receiver functions. Using this model, we systematically vary the strike and dip of the Moho to compute a suite of synthetic receiver functions. The synthetic radial and tangential record sections are then quantitatively compared to the observed record sections. In this manner we attempt to solve for the strike and dip that minimizes the difference between the observed and computed record sections.

Results using this grid search approach for the orientation of the converting interface below the MKAR array were inconclusive. Our analysis revealed that the Moho below the MKAR array is 47 ± 6 km deep. For the KKAR array, the analysis suggested a Moho at a depth 38 ± 5 km with a strike of $N30^\circ E \pm 20$ and a dip of $6^\circ \pm 10$. Results from these exercises indicate that the near-array structure is quite complicated at both arrays, and more research is required into methods that can account for near-array effects in a simple and straightforward manner.

7.2 Analysis of the *PcP* Phase

In another attempt to gain further insight into near-array structure, we examined the *PcP* phase. At far-regional distances, *PcP* arrives with a nearly vertical incidence angle and any moveout across the array should be directly related to the near-array structure. Our plan was to incorporate results from the *PcP* analysis with the receiver function results to provide a clearer picture of the structure below the array. This could lead to a better understanding of the heterogeneity that is important at far-regional distances.

Figure 38 shows the expected slowness and travel-time of the *PcP* phase for far-regional distances. Between $10 - 30^\circ$ distance, *PcP* arrives with phase velocities between 100 and 40 km/s, which at the shorter offsets is essentially vertically incident. It is this feature that we wish to exploit to help better understand non-planar structures situated below the arrays. However, identifying *PcP* can be difficult at far-regional distances for several reasons, including weak amplitudes that are due to the impedance at the core-mantle boundary and potential interference from S-wave arrivals at a distance of $\sim 20^\circ$.

We identified 56 events from our far-regional database that had potentially observable *PcP* arrivals. These events were observed between $12 - 26^\circ$ epicentral distances and had a good overall signal-to-noise quality. In Figure 39 we show a spectrogram of signal windowed around the AK135-predicted *PcP* arrival for an event recorded by the KKAR array at a distance of 16.4° . In this particular example several packets of energy arrive within a 20-second window of the predicted *PcP* arrival. To identify these signals, we applied array-processing methods to find arrivals occurring at near vertical incidence.

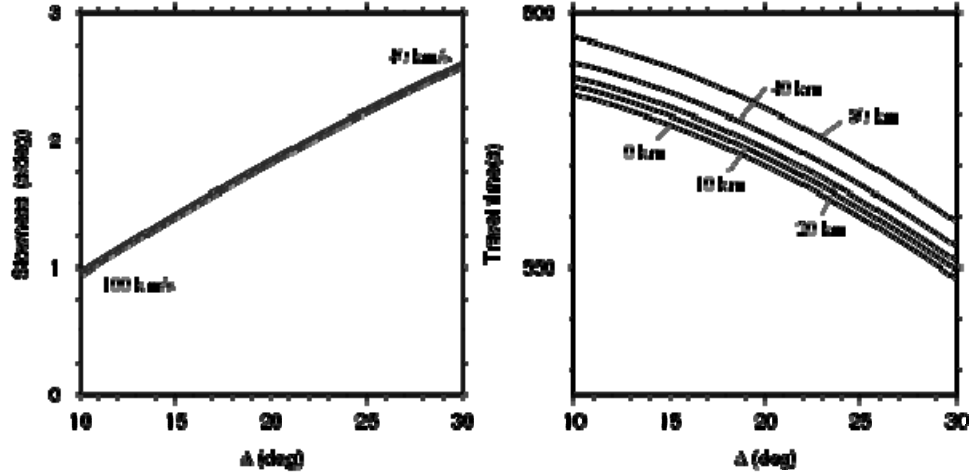


Figure 39. Behavior of the *PcP* phase at far-regional distances. *Left:* Slowness computed for *PcP* for a source at the Earth’s surface using the AK135 reference model; phase velocity at 10° (~100 km/s) and 30° (40 km/s) are labeled. *Right:* The travel-time of *PcP* for source depths of 0, 10, 20, 40 and 80 km.

Figure 40 shows the slowness vespagrams for the event in Figure 39. In this case, we used phase-coherence semblance stacking (described in a previous section) to measure the phase velocities. Most of the energy in the window arrives at high phase velocities indicating a steep incidence to the array. The predominant arrival occurs at ~13 seconds with a velocity of ~45 km/s. This is preceded 6 seconds earlier by a weaker arrival with a similar velocity (both are labeled in Figure 40). Such high phase velocities limit the potential phases these arrivals represent, ruling out *S* arrivals or surface waves.

We processed all 56 events in our data set for *PcP* arrivals. In order to confidently identify these phases, we required observations from several events over a range of distances that exhibited high phase velocities. Out of the 56 events, we were able to find 9 with potential *PcP* arrivals. In some cases, possible *PcP* precursors were also observed, and slower arriving energy in the same time window was interpreted as potential *PcP* converted phases from structure near the array. However, further analysis would be needed to verify these hypotheses.

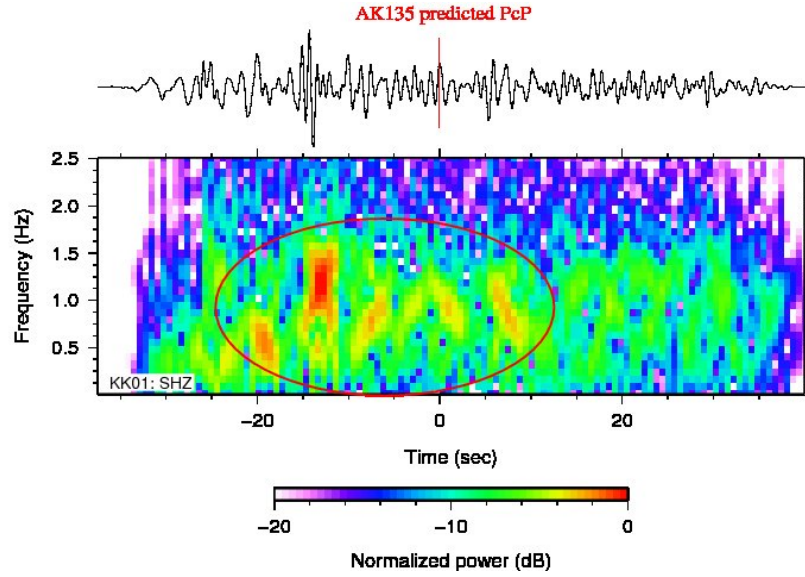


Figure 40. Spectrogram of a seismogram window around the predicted *PcP* phase (zero time). The seismic event was recorded by the KKAR array at a distance of 16.4° and the central array element is shown. Red circle highlight potential *PcP* arrival.

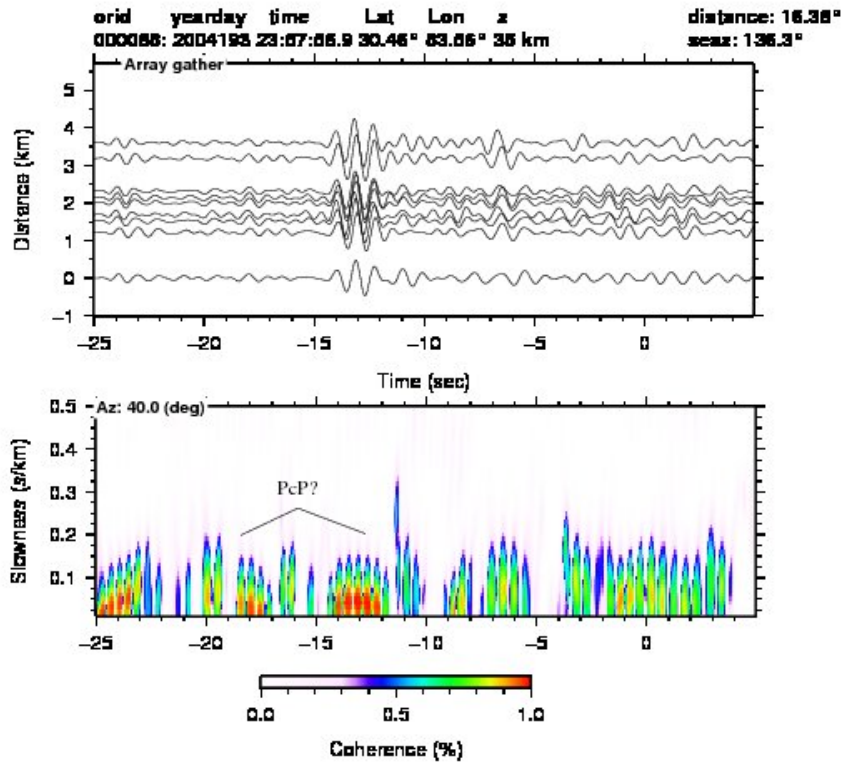


Figure 41. Phase-weighted semblance stacking for *PcP* arrivals. Time axis is the same as Figure 39 . Data were filtered between 0.8 and 1.75 Hz prior to processing. Potential *PcP* arrivals with high phase velocities are labeled.

In order to attempt to deduce information on potentially dipping structure below the arrays we cross-correlated the *PcP* arrivals across the individual arrays to determine the time delay of the phase. Since *PcP* is near vertical at short-offsets, it was assumed that the pattern in the time delays would be directly related to orientation of the non-planar structures below the array. However, for 7 of the 9 events the cross-correlation delay times were 0.0 for most array elements, suggesting that either the structure below the arrays is planar or our assumption concerning *PcP* was incorrect. For the other two events, the cross-correlation delay times could not be fit with a planar surface.

In summary, the near-array structure below MKAR and KKAR appears to be quite complicated. It has a strong affect on back-azimuth residuals ($\pm 20^\circ$) and receiver functions show large amounts of tangential energy. Our attempts to quantify the structure using a single dipping interface were not completely successful. At MKAR we were not able to obtain a reliable solution with such a model from either the polarization analysis, receiver function analysis, or by examining *PcP* arrivals. At KKAR the polarization and receiver-function analysis suggest a Moho that dips to the northeast at $6 - 10^\circ$.

References

- Ambraseys, N., and R. Bilham (2003). Earthquakes and associated deformation in northern Baluchistan 1892-2001, *Bull. Seism. Soc. Am.*, **93**, 1573-1605.
- Barani, S., G. Ferretti, M. Massa, and D. Spallarossa (2007). The waveform similarity approach to identify dependent events in instrumental seismic catalogues. *Geophys. J. Int.*, **168**, 100-108.
- Baljinnyam, I., A. Bayasgalan, B. A. Borisov, A. Cisternas, M. G. Dem'yanovich, I. Ganbaatar and 5 others (1993). Ruptures of major earthquakes and active deformation in Mongolia and its surroundings, *Memoirs of the Geol. Soc. Am.*, **181**, 62 pp.
- Bassin, C., G. Laske, and G. Masters (2000). The Current Limits of Resolution for Surface Wave Tomography in North America, *EOS Trans AGU*, **81**, F897.
- Bayasgalan, A., J. Jackson, and Dan McKenzie (2005). Lithosphere rheology and active tectonics in Mongolia: relations between earthquake source parameters, gravity and GPS measurements, *Geophys. J. Int.*, **165**, 1151-1179.
- Bezdek, J. C. (1981). Pattern recognition with fuzzy objective function algorithms, Plenum Press, New York.
- Billington, S., L. B. Isacks, and M. Barazangi (1977). Spatial distribution of mantle earthquakes in the Hindu Kush-Pamir region: a contorted Benioff zone, *Geology*, **5**, 699-704.
- Bragazangi, M., and J. Ni (1982). Velocities and propagation characteristics of Pn and Sn beneath the Himalayan arc and Tibetan plateau: possible evidence for underthrusting of Indian continental lithosphere beneath Tibet, *Geology*, **10**, 179-185.
- Brazier, R., and A. A. Nyblade (2003). Upper mantle *P* velocity structure beneath the Baikal rift from modeling regional seismic data, *Geophys. Res. Lett.*, **30**, 4, doi:10.1029/2002GL016115.
- Burtman, V., and P. Molnar (1993). Geological and geophysical evidence of deep subduction of continental crust beneath the Pamir, *Geol. Soc. Am. Spec. Pap.*, 281.
- Capon, J. (1969). High-resolution Frequency-wavenumber Spectrum Analysis, *Proc. IEEE*, **57**, 1408-1418.
- Carbonell, R., and S. B. Smithson (1994). Inversion of reflected PP, SS, and converted PS/PP travel times for crustal structure, *Bull. Seism. Soc. Am.*, **84**, 1889-1902.
- Clayton, R., and G. McMechan (1981). Inversion of refraction data by downward continuation, *Geophysics*, **46**, 6860-868.
- Curtis, A., and J. H. Woodhouse (1997). Crust and upper mantle shear velocity structure beneath the Tibetan plateau and surrounding regions from inter-event surface wave phase velocity inversion, *J. Geophys. Res.*, **102**, 11789-11813.
- Engdahl, E. R., R. van der Hilst, and R. Bulland (1998). Global teleseismic earthquake relocation with improved travel times and procedures for depth determination. *Bull. Seism. Soc. Am.*, **88**, 722-733.
- Engdahl, E. R., J. A. Jackson, S. C. Meyers, and E. A. Bergman (2006). Relocation and assessment of seismicity in the Iran region, *Geophys. J. Int.*, **167**, 761-778.

- Emmerson, B., J. Jackson, D. McKenzie, and K. Priestley (2006). Seismicity, structure and rheology of the Lake Baikal region. *Geophys. J. Int.*, **167**, 1233-1272.
- Ferretti, G., M. Massa, S. Solarino (2005). An improved method for the recognition of seismic families: Application to the Garfaguana-Lunigiana Area, Italy, *Bull. Seism. Soc. Am.*, **95**, 1903-1915.
- Gao, S., K.J Lui, and C. Chen (2004). Signification crustal thinning beneath the Baikal rift zone: new constraints from receiver function analysis, *Nature*, **31**, doi:10.1038/nature03143.
- Hetzel, R., M.X. Tao, S. Stokes, S. Niedemann, S. Ivy-Ochs, B. Gao, M.R. Strecker and P.W. Kubik (2004). Late Pleistocene/Holocene slip rate of the Zhangye thrust (Qilian Shan, China) and implications for the active growth of the northeastern Tibetan plateau, *Tectonics*, **23**, TC6006, doi:10.1029/2004TC001653.
- International Seismological Centre (ISC) (2001). *On-line Bulletin*, <http://www.isc.ac.uk>, Thatcham, United Kingdom.
- Jackson, J., K. Priestley, M. Allen, and M. Berberian (2002). Active tectonics of the south Caspian Basin, *Geophys. J. Int.*, **148**, 214-245.
- Kennett, B. L. N. (1988). Systematic Approximations to the Seismic Wave Field, Chapter III.1 in *Seismological Algorithms*, ed. D. J. Doornbos, Academic Press.
- Kennett, B. L. N., and E. R. Engdahl (1991). Travel times for global earthquake location and phase identification, *Geophys. J. Int.*, **105**, 429-465.
- Kennett, B. L. N., E. R. Engdahl, and R. P. Buland (1995). Constraints on seismic velocities in the earth from traveltimes, *Geophys. J. Int.*, **122**, 108-124.
- Kosarev, G., N. Petersen, L. Vinnik and S. Roecker (1993). Receiver functions for the Tien Shan analog broadband network: contrasts in the evolution of structures across the Talasso-Fergana Fault, *J. Geophys. Res.*, **98**, B3, 4437-4448.
- Langin, W. R., L.D . Brown and E. A. Sandvol (2003). Seismicity of central Tibet from project INDEPTH III seismic recordings, *Bull. Seism. Soc. Am.*, **93**, 2146-2159.
- Leech, M. L., S. L. Klemperer, and W. D. Mooney, eds., (2010), *Proceedings of the 25th Himalaya-Karakoram-Tibet Workshop: U.S. Geological Survey Open-File Report 2010-1099*.
- Maggi, A., J. A. Jackson, K. Priestley and C. Baker (2000). A re-assessment of focal depth distributions in southern Iran, Tien Shan and northern India: do earthquakes really occur in the continental mantle?, *Geophys. J. Int.*, **143**, 629-661.
- Mangino, S., and K. Priestley (1998). The crustal structure of the south Caspian region, *Geophys. J. Int.*, **133**, 630-648.
- McNamara, D.E., W.R. Walter, T.J. Owens, C.J. Ammon (1997). Upper mantle velocity structure beneath Tibet Plateau from Pn travel time tomography, *J. Geophys. Res.*, **102**, 493-505.
- McMechan, G. A. (1984). Inversion of a refraction wavefield by imaging in the p-x and v-z planes, *Geophys. J. R. Astr. Soc.*, **78**, 723-733.

- McMechan, G.A. and R. Ottolini (1980). Direct observation of a p - τ curve in a slant stacked wave field, *Bull. Seism. Soc. Am.*, **70**, 775-789.
- Menke, W. (1999). Using waveform similarity to constrain earthquake location, *Bull. Seism. Soc. Am.*, **89**, 1141-1146.
- Morozov, I. B., E. A. Morozova, and S. B. Smithson, P. G. Richards, V. I. Khalturin, and L. N. Solodilov (2005). 3D first arrival calibration model for northern Eurasia, *Bull. Seism. Soc. Am.*, **95**, 951-964.
- Niazi, M. (1966). Corrections to apparent azimuths and travel-time gradients for a dipping Mohorovicic discontinuity, *Bull. Seism. Soc. Am.*, **56**, 491-509.
- Paul, A., A. Kaviani, D. Hatzfeld, J. Vergne and M. Mokhtari (2006). Seismological evidence for crustal-scale thrusting in the Zagros mountain belt (Iran), *Geophys. J. Int.*, **166**, 227-237.
- Pegler, J.P. and S. Das (1998). An enhanced image of the Pamir-Hindu Kush seismic zone from relocated earthquake hypocenters, *Geophys. J. Int.*, **134**, 573-595.
- Petit, C., J. Deverchere, E. Calais, V. San'kov, D. Fairhead (2002). Deep structure and mechanical behavior of the lithosphere in the Hangai-Hovsgol region, Mongolia: new constraints from gravity modeling, *Earth and Plan. Sci. Lett.*, **197**, 133-149.
- Priestley, K., E. Debayle, D. McKenzie and S. Pilidou (2006). Upper mantle structure of eastern Asia from multimode surface waveform tomography, *J. Geophys. Res.*, **111**, B10304, doi:10.1029/2005JB004082.
- Quittmeyer, R. C. and K. H. Jacobs (1979). Historical and modern seismicity in Pakistan, Afghanistan, northwestern India, and southeastern Iran, *Bull. Seism. Soc. Am.*, **69**, 3, 773-823.
- Roecker, S. W. (1982). Velocity structure of the Pamir-Hindu Kush region: possible evidence of subducted crust, *J. Geophys. Res.*, **87**, 947-959.
- Rost, S., and C. Thomas (2002). Array seismology: methods and applications, *Rev. Geophys.*, **40**, doi:10.1029/2000RG000100.
- Schimmel, N., and H. Paulssen (1997). Noise reduction and detection of weak, coherent signals through phase weighted stacking, *Geophys. J. Int.*, **130**, 497-505.
- Searle, M., B. R. Hacker and R. Bilham (2001). The Hindu Kush seismic zone as a paradigm for the creation of ultrahigh-pressure diamond and coesite bearing continental rocks, *J. Geol.*, **109**, 143-153.
- Stoica, P., and A. Nehorai (1989) Music, maximum likelihood, and Cramer-Rao lower bound, *IEEE Trans. Acoust. Speech Signal Process.* **37**, 720-741.
- Suvorov, V., Z. M. Mishenkina, G. V. Petrick, I. F. Sheludko, V. S. Seleznev, V. M. Solovyov (2002). Structure of the crust in the Baikal rift zone and adjacent areas from deep seismic sounding data, *Tectonophysics*, **351**, 61-74.
- ten Brink, U. S., and M. H. Taylor (2002). Crustal structure of central Lake Baikal: insights into intracontinental rifting, *J. Geophys. Res.*, **107**, doi:10.1029/2001JB000300.
- Tatar, M., D. Hatzfield, M. Ghafory-Ashtiany (2004). Tectonics of the Central Zagros (Iran) deduced from microearthquake seismicity, *Geophys. J. Int.*, **156**, 255-266.

- Talebian, M. and J. Jackson (2004). A reappraisal of earthquake focal mechanisms and active shortening in the Zagros mountains of Iran, *Geophys. J. Int.*, **156**, 506-526.
- Tibuleac, I. M. and E. T. Herrin (1997). Calibration studies at TXAR, *Seism. Res. Lett.*, **68**, 353-365.
- VanDecar, J. C. and R. S. Crosson (1990). Determination of teleseismic relative phase arrival times using multi-channel cross-correlation and least squares, *Bull. Seism. Soc. Am.*, **80**, 150-159.
- Walker, R., and J. Jackson (2004). Active tectonics and late Cenozoic strain distribution in central and eastern Iran, *Tectonics*, **23**, doi:10.1029/2003TC001529.
- Walker, R.T., A. Bayasgalan, R. Carson, R. Hazlett, L. McCarthy, J. Mischler, E. Molor, P. Sarantsetseg, L. Smith, B. Tsogtbadrakh and G. Tsolmon (2006). Geomorphology and structure of the Jid right-lateral strike-slip fault in the Mongolian Altay mountains, *J. Struct. Geol.*, **28**, 1607-1622.
- Zhou, H. W. and M. A. Murphy (2005). Tomographic evidence for the wholesale underthrusting of India beneath the entire Tibetan plateau, *J. Asian Earth Sci.*, **25**, 445-457.
- Zugibe, T. P., S. D. Frank and A. Ferris (2008). Crustal structure of the Pakistan Himalayas from receiver functions, *Abstract, SSA Annual Meeting, Sante Fe, New Mexico*.

Appendix 1: Altering Small-Aperture Array Geometry to Improve Phase-Velocity Estimation

A major focus of this project was the development of analysis methods to process far-regional arrivals observed on small-aperture arrays. By analyzing the array response functions, we know that the small array apertures of MKAR and KKAR produce a lack of precision in slowness and back-azimuth estimates, and the inter-sensor spacing creates wave-number aliasing that reduces accuracy in the slowness estimate. In this appendix we show that significant improvements in slowness resolution can be gained by analyzing data from a sub-array from the current MKAR and KKAR configuration, or by adding a single, optimally placed array element at some distance away from the center of the array.

For example, Figure A-1 shows the current configuration of the KKAR array (black triangles), which has nine elements and a total aperture of ~ 3.5 km. At far-regional distances, the P arrivals travel across the array at phase velocities between $8.0 - 12.0$ km/s, requiring only $0.27 - 0.44$ seconds to traverse the full aperture of the array, and the travel time between adjacent array elements is even smaller. While the small differential travel time across the array allows for high signal coherence between array elements, it also negatively affects the quality of beam-forming results, which involve time shifting and stacking to find the directional parameters. This makes distinguishing a Pn_l arrival, or a depth phase, from a $P410$ arrival, extremely difficult with slowness (or phase velocity) measurement alone. The lack of precision and resolution is a consequence of the small time shifts required between array elements to span the phase velocity range of $8.0 - 12.0$ km/s during the beam-forming process. The small time shifts do not significantly affect the power or coherency in the beam stack, and hence the confidence regions in arrival measurements span a large range of slowness and back-azimuths.

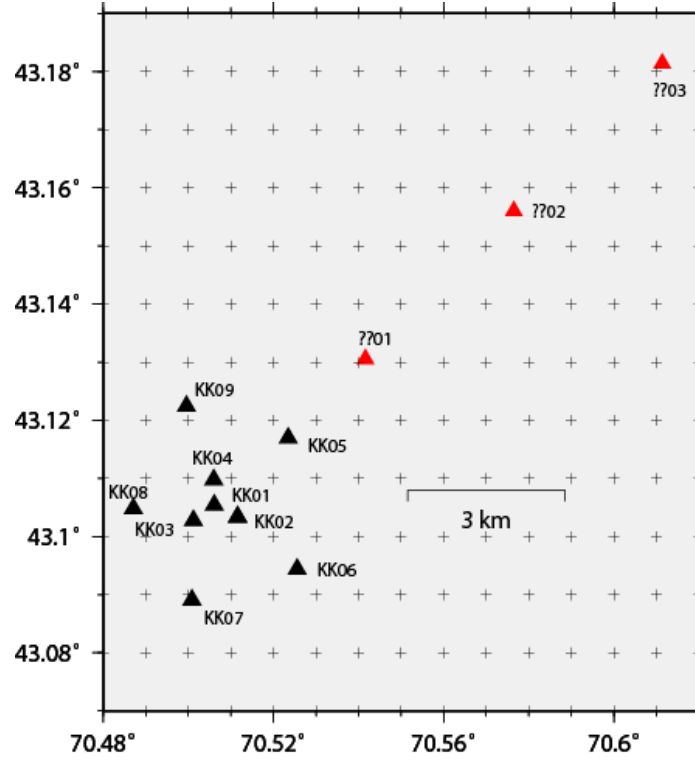


Figure A-1. Black triangles depict the current configuration of the KKAR array; the red triangles are hypothetical stations positioned at 4, 8 and 12 km from the center of the current array.

To demonstrate the usefulness of altering small-aperture array geometry, we performed vespagram analysis of synthetic *P*-wave seismograms generated using various array configurations. We modeled the wavefield for a point-source dislocation in Iran as it would be observed at KKAR at a distance of 16° and a back azimuth of 225° . We examined the vespagrams results for several cases, including the full array, and sub-arrays with or without additional outer elements. This hypothetical example represents a best-case scenario, since the synthetic data do not contain noise, and the *P* arrival is a single well-defined pulse (Figure A-2).

Array Configuration 1: Vespagram Analysis using Sub-arrays

In Figure A-3 we show the results of applying 4th-root vespagrams analysis to two configurations of the current KKAR array. Figure A-3a shows the results using all nine elements of the KKAR array, and these can be compared to the results in Figure A-3b, which were computed using only the five outer array elements of the KKAR array. For this synthetic example, the vespagram in Figure A-3b is more peaked. This occurs because the beam power built up by the contribution of the inner elements to the waveform stack changes little for different phase-velocity time-shifts, due to spatial closeness of the array elements. In essence, using all the inner elements over-weights the stack and produces the phase-velocity smearing seen in Figure A-3a. We note that both vespagram analyses produced the correct phase velocity of 8.5 km/s for the initial *P* arrival. The sharpness of the peaks in phase velocity is best illustrated with slices taken through $t = 0.825$ s in each vespagram; these are shown in Figure A-5 for all the examined cases.

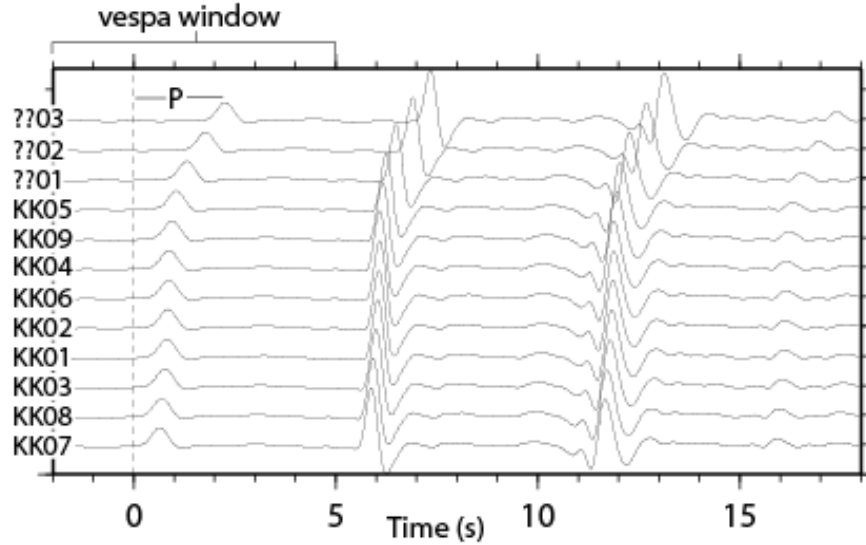


Figure A-2. Synthetic array gather for the current configuration of KKAR and three additional hypothetical stations (labeled as ??01, ??02, and ??03). Waveforms were generated from a point source in Iran, at a distance of 16° and back azimuth of 225° from KKAR. The waveforms are aligned based on their moveout with respect to the closest station to the event (KK07 in this case). The *P* arrival and the vespa analysis window are indicated near the top of the plot.

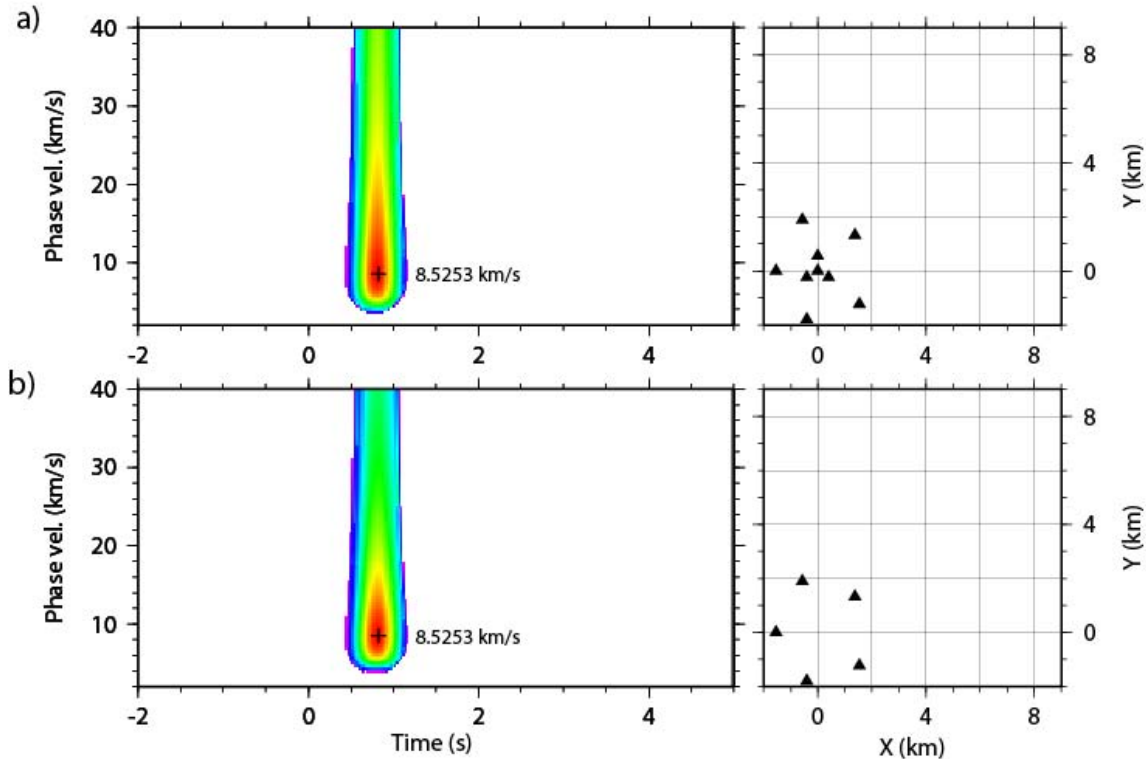


Figure A-3. Vespagram analysis of the *P* arrivals in the synthetic waveforms in Figure A-2. a) results computed using all nine elements of the array (shown to the right); b) results computed using only the outermost five elements of the array; the phase velocity is more sharply defined.

Array Configuration 2: Vespagram Analysis with Additional Elements

For this case we illustrate the effect that increasing the overall array aperture has on the performance of the vespagram method. By increasing the array aperture, the travel time across the array for the body-wave arrivals also increases, which subsequently improves the phase velocity estimate. Adding a station outside the current array at carefully chosen azimuths can also significantly improve phase-velocity resolution for events in regions of interest. For example, in Figure A-4 we show the vespagrams computed with the outer ring of elements at KKAR and a single array element at 4, 8, or 12 km from the center of the array along the great-circle path from the event to the southwest (red stations in Figure A-1). The phase-velocity peaks become sharper as the distance of the additional element increases from the center of the array. Adding a station 4 km from the array center (Figure A-4a) removes a significant portion of the velocity smearing seen in the original analysis in Figure A-3a. The least amount of phase-velocity smearing is seen when a station is added at 8 (Figure A-4b) or 12 km (Figure A-4c) from the array center. However, in a real world scenario, site noise and structural heterogeneity around the array would limit the maximum beneficial distance of the added station, since maintaining signal coherence across the array is also very important for array performance. We also note that expanding the array aperture without adding other interior array elements can cause unwanted spatial aliasing. However, both of the scenarios included here produce a vespagram with little smearing at high phase velocities. Figure A-5 shows the narrow (well-resolved) peaks in phase velocity produced by the adding single elements at various distances.

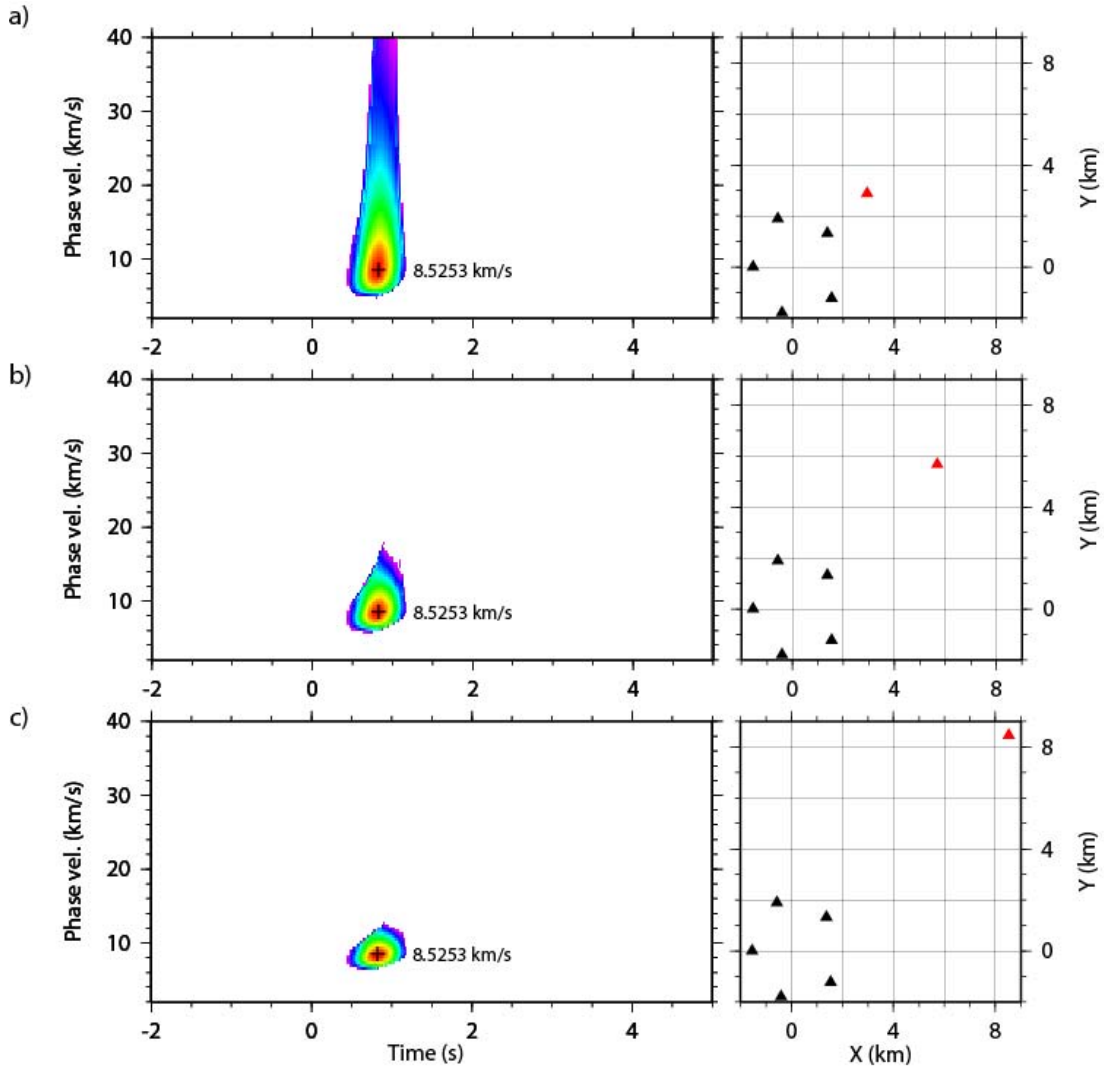


Figure A-4. Vespagrams for the *P* arrival in Figure A-2, using the five outer elements of the array and an additional hypothetical station at a) 4 km; b) 8 km; and c) 12 km from the center of the array and along the great-circle path from the event. As the distance between the station and array increases, the *P* phase velocity becomes significantly easier to pick with confidence.

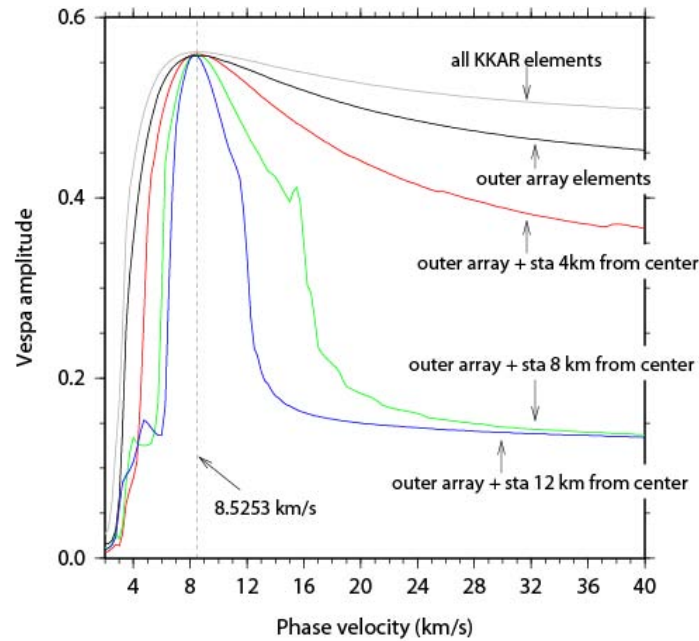


Figure A-5. Profile comparisons of the vespagrams shown in Figures A-3 and A-4. The color-coded lines are profiles taken through the $t = 0.825$ s in each vespagram. While all profiles have their absolute peak at the correct phase velocity (8.5253 km/s), the phase-velocity resolution is improved by increasing the array aperture.

In summary, the small aperture of regional arrays such as KKAR limits the velocity resolution for events observed at distances between $13 - 30^\circ$. At these distances, multiple arrivals occur in short time windows, and the velocity resolution becomes critically important to differentiate between them. While our analysis was limited to synthetic data, it appears that the resolution in phase velocity can be improved by simply limiting the number of inner array elements used in vespagram analysis. However, the greatest improvement occurs when stations are added outside of the current array configuration. While we did not determine the optimal array configuration to analyze all intermediate-distance events, the examples shown here suggest that adding 3 to 5 array elements at 8 – 12 km distance from the array center would significantly improve array analysis methods for events at this distance range.